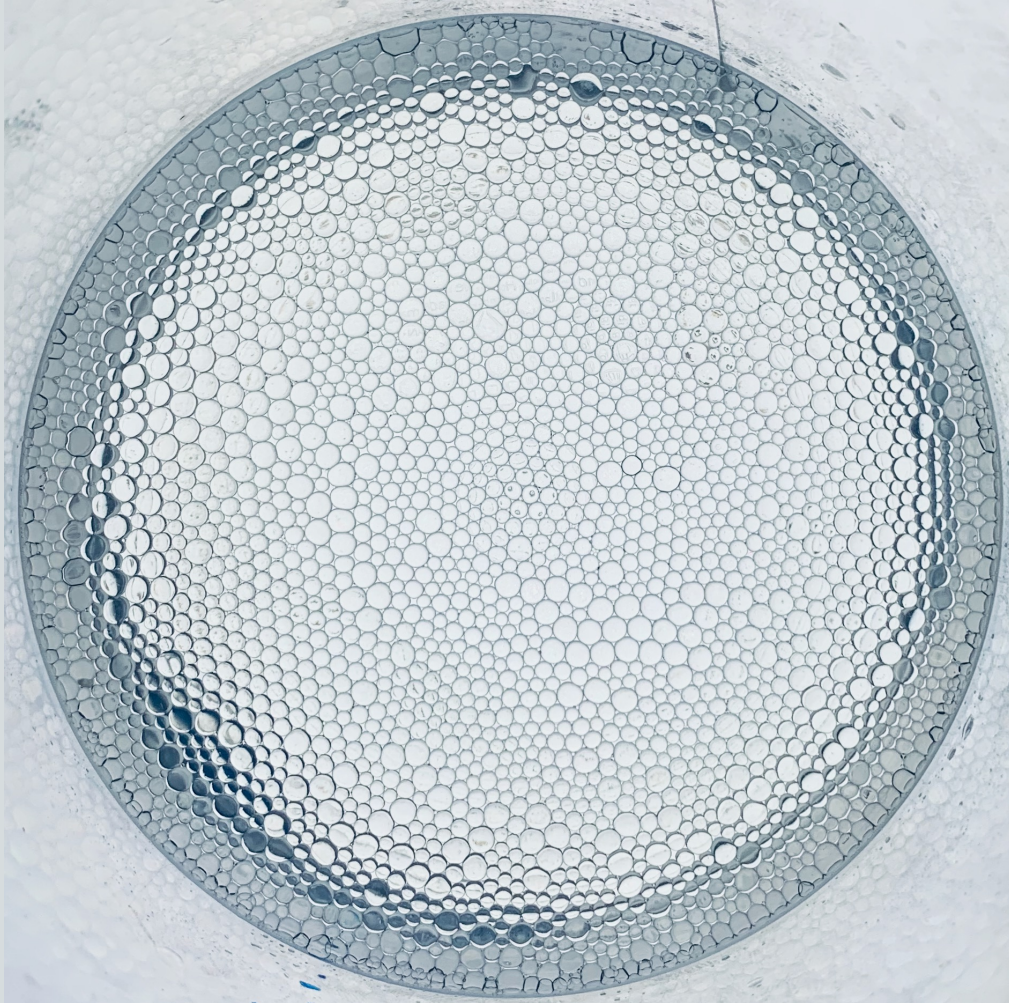


Rheology of Emulsion Monolayers



Author:
Ning Ji

Supervisors:
Dr. Daniel S.W. Tam
Dr. Brian P. Tighe

Rheology of emulsion monolayers

by

Ning Ji

to obtain the degree of Master of Science
at the Delft University of Technology
to be defended publicly on Tuesday, August 29, 2023 at 10:00

Student number: 5565588

Project Duration: November 21, 2022 - August 29, 2023

Thesis committee:	Dr. D. Tam,	TU Delft, supervisor
	Dr. B. P. Tighe,	TU Delft, supervisor
	Dr. V. Garbin,	TU Delft, committee member
	Dr. E. B. A. Hinderink,	TU Delft, committee member

An electronic version of this thesis is available at <http://repository.tudelft.nl/>.



Copyright © Ning Ji, 2023
All rights reserved.

Abstract

Emulsions, characterized as a metastable dispersion of one liquid into a second one in the presence of surface-active agents, have complex rheology that interests both physicists and industries. Depending on the volume fraction of the dispersed phase (ϕ), emulsions can display both solid-like and liquid-like behavior. Rheometrical measurements of complex fluids usually yield several flow curves, each corresponding to a certain volume fraction. Scaling analysis assists in investigating the fundamental traits of those flow curves by rescaling the rheometrical data onto several master curves described by a few non-dimensional variables.

Whereas experiments successfully scaled the data onto master curves are usually of three-dimensional complex fluids, many numerical simulations are of low-cost two-dimensional flows, lacking direct referable experimental data. Additionally, scenarios involving droplets, bubbles, and particles trapped at the interface of two fluids inherently constitute a two-dimensional system. Motivated by these considerations, the project aims to measure the rheology of emulsion monolayers.

A cylindrical Couette ring configuration was built to facilitate the generation of monolayers and rheometrical measurements. The image processing method was developed to deal with three distinct scenarios, high ϕ , medium ϕ , and low ϕ , depending on the concentration of droplets. The steady velocity profiles and the averaged packing fractions were acquired through image analysis. Subsequently, the local rheology was deduced and compared with the macroscopic rheological measurement at various packing fractions. While the densely packed emulsion monolayer is a shear-thinning yield stress material, the spatial cooperativity (non-local effect) and capillary force (wall effect) were found to have a profound influence on the rheology.

Acknowledgements

I would like to first thank my thesis supervisors - Daniel, for providing me with a first glimpse into experimental fluid research, for being able to understand my ideas even when I struggled to articulate them, for trusting and leaving me a lot of flexibility in my research, and Brian, for his knowledgeable and clear explanations helping me grasp the rheology of complex fluids, for his patience with my endless questions, and for his inspiration and encouragement that kept me motivated during confusing times. I'd also like to thank Yikai for our insightful discussions on experiments and for sharing the joys and frustrations of research in daily chats. Thanks to Bob, for guiding my initial experiment, encouraging my attempts in image processing, and always being willing to share lab and coding tricks.

I would like to thank my friends at TU Delft. Beyond satisfying my appetite as a foodie, your companionship has provided me with the spiritual nourishment that reminds me of life's joys, even during my most challenging times. Thank you to my parents, for your constant support and concern for my physical and mental health, even though I haven't been home for two years.

Contents

List of Figures	ix
List of Tables	xiii
1 Motivation	1
1.1 Introduction	1
1.2 Research objectives	2
2 Background	3
2.1 Rheology	3
2.1.1 Viscosity	3
2.1.2 Viscoelastic	4
2.1.3 Rheological measurement	5
2.2 Emulsion	6
2.3 Universal scaling analysis	6
2.3.1 Methodology of universal scaling analysis on flow curves	9
2.4 Two dimensional experiments on complex fluids	11
2.5 Experimental set-up for interfacial rheology	14
3 Experimental setup and methods	17
3.1 Design Targets	17
3.2 Experimental setup	17
3.2.1 Couette-ring cup	18
3.2.2 Background illumination system	19
3.2.3 Emulsion preparation	20
3.3 Experimental methods	21
3.3.1 Measurement duration	22
3.3.2 Low torque adjustment	23
3.3.3 Range of $\dot{\Omega}$ and ϕ	24
3.3.4 Final experiments	26
4 Image analysis	29
4.1 Image processing of single frame	30
4.1.1 Binarization and morphological operation	30
4.1.2 Large void mask	33
4.1.3 Validation: droplet identification	34
4.1.4 Validation: packing fraction	34
4.2 Velocity profile: frame correlation	35
5 Results and discussions	39
5.1 Packing fraction ϕ	39
5.2 Velocity profile	41
5.3 Macroscopic and local flow curves	42

6 Conclusion and Outlook**49****References****54**

List of Figures

2.1	(a) Flow curves $\sigma(\dot{\gamma})$ of a shear thinning (green), Newtonian (black), and shear thickening (red) fluid. (b) Typical behavior of a shear thinning liquid with zero shear viscosity (black) and yield stress (orange) (Figure reproduced from [21]).	4
2.2	Measuring geometries: (a) cone-plate, (b) plate-plate and (c) Couette.	5
2.3	Shear stress versus strain rate given several different volume fractions (a) for colloidal gel particles (Figure reproduced from [9]). The fluid is driven through the microfluidic channel by the pressure gradient. The dashed lines are fit to the Hershel-Bulkley model, while the subcritical cases exhibit no yield stress and reduce approximately to a power law. (b) for castor oil emulsion sheared in a cone-plate geometry. The solid lines represent the Herschel-Bulkley fit and in the subcritical branches are the Cross fit. Black symbols and blue symbols correspond to samples with $\phi > \phi_c$ and $\phi < \phi_c$ respectively. (Figure reproduced from [10])	7
2.4	Master curve showing collapse of flow curves onto two branches, one for samples with $\phi > \phi_c$ and one for samples with $\phi < \phi_c$ when plotted as $\sigma/ \Delta\phi ^\Delta$ versus $\dot{\gamma}/ \Delta ^\Gamma$ (a) for colloidal gel particles (Figure reproduced from [9]). The first exponent uncertainties are statistical; the second are systematic. (b) for castor oil emulsion sheared in a cone-plate geometry. Inset: Fit of the Newtonian viscosity to the Krieger-Dougherty equation, giving $\eta_s = 2.2 \times 10^{-3} \text{Pa} \cdot \text{s}$ and $m = 1.71$ with $\phi_c = 0.645$. (Figure reproduced from [10])	8
2.5	Velocity profiles (a) for bidisperse foam confined in a Hele-Shaw geometry with inner wall rotating (\bullet : $\phi = 0.80$; \blacktriangle : $\phi = 0.88$; \blacklozenge : $\phi = 0.95$). Note that it's a log scale plot and the small plateau for $0 < r < 1$ corresponds to first row of bubbles, not shear rate discontinuity. (Figure reproduced from [37]) (b) for bidisperse bubble raft in a cylindrical Couette configuration with outer wall rotating at $\Omega = 5 \times 10^{-3} \text{rad/s}$ (\bullet) and $\Omega = 8 \times 10^{-3} \text{rad/s}$ (\blacksquare). The inset shows a close look at the discontinuity of shear rates. (Figure reproduced from [17])	11
2.6	Velocity profiles for the bidisperse foam sheared in a Taylor-Couette geometry (a) with top plate: the curves exhibit strong shear banding and rate-dependence. (b) without top plate: the curves are approximately rate-independent velocity profiles and the shear banding is due to the curved geometry (Figures reproduced from [40]).	13
2.7	Velocity profiles for the linearly sheared <i>monodisperse</i> foams (a) without top plate: the curves are close to linear; (b) with top plate: the curves show strong shear banding behavior (Figures reproduced from [18]). Note that both cases result in rate-independent velocity profiles.	13

2.8	(a) Velocity profiles of the linearly sheared <i>monodisperse</i> foam with a top plate, exhibiting rate-independence for 0.083mm/s (black curve), 0.26mm/s (dark gray curve), and 0.83mm/s (light gray curve). (b) Velocity profiles for the linearly sheared <i>bidisperse</i> foam with a top plate, which is rate dependent. Figures are reproduced from [46].	14
2.9	(a) Corss section of bi-cone geometry (Figure reproduced from [47]). (b)Cross section of the DWR setup (Figure reproduced from [20].	15
3.1	Sketch of Couette ring configuration used in this experiment.	18
3.2	(a) A SolidWorks model of the slanted cup wall. The cup and the mirror support are connected by screws. (b) An image of the shadow region caused by light refraction in a normal beaker with a vertical wall. (c) A photo of the PDMS ring (dark blue) used to seal the gap between the 3d printed cup wall and the acrylic cup bottom.	19
3.3	(a) A SolidWorks model of the background illumination system. From top to bottom are a centering ring, a diffusing paper, a glass diffuser, a reflecting paper, a LED stripe, a container and a connector to the rheometer. (b) An example of the experimental image.	20
3.4	(a) The distribution of droplet diameters over one revolution at rotational speed $\dot{\Omega} = 0.0086$ (rad/s). The bidisperse monolayer consists of droplets of 1.4 ± 0.1 and 1.9 ± 0.1 mm diameter, with an average diameter $\langle d \rangle = 1.6$ mm for all droplets. (b) An experimental photo of two vertical needles with different diameters. (c) A sketch of the deviation angle from the horizontal plane.	21
3.5	Torque measurements over twelve revolutions at different rotational speeds: $\dot{\Omega} = 0.3479, 0.1210, 0.0421$ (rad/s) respectively. The x-axis represents time normalized by the rotational speed, where 12 revolutions are equivalently represented by 24π . The y-axis is the measured torque, with varying ranges in the three plots: as the rotational speed decreases, the measured torque also decreases. The blue solid line represents the original data at a measurement frequency of 10 Hz, with the removal of outliers using a Hamper identifier. The red dashed line is the smoothed data obtained by filtering the measurements through a Savitzky-Golay finite impulse response (FIR) smoothing filter, which reveals 12 repeating periods.	22
3.6	Comparison of torque measurements in two independent experiments: experiment A was performed without motor adjustment given $\phi = 0.9213 \pm 0.0039$ and experiment B was performed with motor adjustment given $\phi = 0.9188 \pm 0.0043$. (a) Torque measured over one revolution at a low rotational speed $\dot{\Omega} = 0.0030$ (rad/s). The left plot presents the results of experiment A, featuring a negative torque region and six smaller periods within one revolution. In contrast, the right plot displays the results of experiment B, demonstrating a more consistent trend within one revolution, attributed to the application of motor adjustment. The steady torque of two measurements vary significantly. (b) Torque measured over one revolution at a high rotational speed $\dot{\Omega} = 0.2052$ (rad/s). The steady torques of two experiments are comparable.	23
3.7	Steady torque vs. rotational speed (blue square) with packing fraction $\phi = 0.9537 \pm 0.0023$. The yellow line represent the lowest rotational velocity chosen for the final measurement, and the red line represents the highest.	24

3.8	Torque evolution over the droplet-filling process, mixing at a constant rotational speed 0.25 (rad/s). The red pentagram represents the first time for stopping the pump.	25
3.9	The experimental image for the first measured droplet packing at (a) the highest rotational speed. (b) the lowest rotational speed.	26
4.1	Three components of an experimental image: the aqueous background, the droplet interior, and the droplet edge.	29
4.2	Single-frame processing. A-C: original, filtered and binary image; D: small-area filtered image; E.1-3: watershed and morphological operation; F: histogram equalization; G.1-3: steps of masking large voids.	31
4.3	Validation of droplet identification and packing fraction. The first column presents original images with the droplet centers detected. The corresponding binary images are shown in the second column. The third column depicts the area fraction occupied by droplets within the black fan-shaped region.	32
4.4	Steps for removing large gaps in the low ϕ scenario.	33
4.5	Validation of frame correlation. On the right are the zoom-in views of the inner, the middle, and the outer regions.	35
4.6	The sketch of a one-dimensional staggered grid for a discrete description of steady azimuthal velocity and local shear rates.	36
4.7	The velocity normalized by the rotational velocity v_0 versus the normalized radius. (a) A comparison between different bin numbers. (b) A comparison between different frame rotational speeds.	37
5.1	Average packing fraction profile in one revolution.	39
5.2	(a) Sketch of the small ROI (pink part) with the range $\{38.0 \leq r \leq 45.8 \text{ (mm)}, -28 \leq \theta \leq 28 \text{ (}^\circ)\}$; the result is labeled as ϕ^s . (b) Sketch of the large ROI (blue part) with the range $\{36.5 \leq r \leq 47.3 \text{ (mm)}, -43 \leq \theta \leq 43 \text{ (}^\circ)\}$; ϕ^l denotes the emulsion packing fraction in this region. (c-d) Distribution of the packing fractions in azimuthal direction. The subscripts are consistent with those in the Table 3.2.	40
5.3	Packing fractions at different rotational speeds. Different symbols represent different droplet packings.	41
5.4	(a) The steady azimuthal velocity profiles at different rotational speeds (represented by different colors) for $\phi = 0.9468$. The vertical coordinate is the velocity normalized by the inner wall speed, i.e., $v_0 = \Omega R_i$; the horizontal coordinate is the normalized radius with respect to the average diameter of droplets. Plots of other droplet packings are shown in Figure 5.7. (b) The steady azimuthal velocity profiles for various droplet packings (represented by various symbols) at the same rotational speed. For plots of other rotational speeds, see Figure 5.8.	41
5.5	The flow curves at the inner wall. The shear rates are calculated with a Newtonian flow assumption.	42
5.6	(a) The local flow rates. (b) The local flow curves. The green dashed line represents the relation between the shear stress (derived from the Torque measurement) and the shear rate (assuming a Newtonian flow) at the inner wall. The local flow curves for other droplet packings are summarized in Figure 5.10.	43

5.7	Velocity profiles at different rotational speeds (represented by different colors) for a given droplet packing (expressed by various symbols).	44
5.8	Velocity profiles for various droplet packings (represented by various symbols) at a given rotational speed (expressed by different colors).	45
5.9	Local shear rates at different rotational speeds (represented by different colors) for a given droplet packing (expressed by various symbols).	46
5.10	The local flow curves for various droplet packings.	47

List of Tables

2.1	Scaling exponents collected from experiments and simulations for systems with various interparticle interactions. All experiments are three-dimensional and give similar predictions, $\Delta \approx 2$, $\Gamma \approx 4$, $\beta \approx 0.5$ and $\phi_c \approx 0.64$. Nevertheless, numerical simulations with different interparticle interactions and dimensions give various predictions for exponents. Note that the most “classic” mixture of bidisperse packings is that large and small disks with a 1.4:1 ratio of their radii are mixed in equal amounts [34]. The elastic forces between particles are modeled as “one-sided springs”: $f_{el} \sim \delta_{el}^\alpha$, where δ is the dimensionless compression of the spring and $\alpha = 1(3/2)$ corresponds to harmonic (Hertzian) forces [35].	9
3.1	Rotational speeds and corresponding rotational velocities measured for each volume fraction. Each measurement began with the highest speed.	27
3.2	Volume fractions covered in the experiments.	27

Motivation

1.1. Introduction

An emulsion is a metastable dispersion of one liquid into a second one in the presence of surface-active agents [1]. Emulsions are of two types, depending in principle on the nature of the dispersed phase and which kind of liquid forms the continuous phase: oil-in-water (O/W) and water-in-oil (W/O) [2]. Other more complex emulsions are termed multiple emulsions, in which the droplets of the dispersed phase themselves comprise emulsions. In many industries, including foods, cosmetics, paints, pharmaceuticals, biological systems and other household products, emulsions are commonly used and may be encountered throughout all stages of the industrial process, both desirably and undesirably [3]. In the petroleum industry, for instance, produced water from crude oil extraction, which consists mainly of an emulsion, has significant environmental consequences and is in great demand for advanced treatment techniques [4].

Emulsions are complex systems. The measurement, adjustment, and prediction of the flow properties of emulsions have long been of interest to physicists and industry [5]. In industrial applications, the rheology of emulsions is vital and must be tuned to meet the requirements of the products or processes [6]. For example, the stability of an emulsion is strongly associated with its flow properties, which affects the product quality in the food, cosmetic and pharmaceutical industries [7]. At a fundamental research level, obtaining a rigorous quantitative description of the flow properties of emulsions is challenging. Emulsions can exhibit both solid-like and liquid-like behavior depending on the volume fraction of the dispersed phase (ϕ). Below a critical value ϕ_c , emulsions display non-Newtonian flow behavior. However, when ϕ exceeds ϕ_c , emulsions become solid-like and only begin to flow when the yield stress is surpassed. This transition from fluid-like to solid-like behavior is known as jamming, and the critical volume fraction ϕ_c corresponds to the jamming point J . Similar rheological behavior is observed for other complex fluids with the dispersion of one substance in a continuous phase, such as liquid foams, colloidal suspensions and granular media [8]. Despite the fact that these complex fluids are composed of substances with vastly varied physicochemical properties and length scales, researchers are interested in determining whether there are generic descriptions for their rheological properties.

Rheometrical measurements of complex fluids usually yield several flow curves, each corresponding to a certain volume fraction. One possible approach is to describe the flow curves with several dimensionless variables, where the rheometrical data collapse onto several master curves. Nordstrom et al. [9] and Paredes et al. [10] have successfully scaled their experimental steady-flow data with respect to the distance to ϕ_c , $\Delta\phi = \phi - \phi_c$, into two master curves for soft-colloid and emulsion systems, respectively. These master curves are plotted as $\sigma/|\Delta\phi|^\Delta$

versus $\dot{\gamma}/|\Delta\phi|^\Gamma$, and the scaling exponents for the two systems are the same within numerical uncertainty, with $\Delta \approx 2$ and $\Gamma \approx 4$. Similar results have been shown by Basu et al. [11] and Dinkgreve et al. [12] for other complex systems, which further confirms the universality of the flow properties near and across the jamming point of complex fluid systems with different interparticle interactions. The advantage of this scaling approach is that the flow properties of complex fluids can be predicted using a small number of crucial variables, which allows for the identification of universal flow behavior and can be used to better understand the underlying physics of these systems. On the other hand, numerous simulations [13, 14, 15] have investigated the universality of the scaling as well, but their scaling exponents tend to differ from experiments. These differences might indicate that the model of the numerical simulation does not fully describe the experimental interparticle interactions [16].

Whereas experiments successfully scaled the data onto master curves are usually of three-dimensional complex fluids, many numerical simulations are of low-cost two-dimensional flows, lacking direct referable experimental data. Several two-dimensional experiments [17, 18, 19] have been performed to investigate the rheology of complex fluids and successfully fitted experimental data with appropriate models, where 2D configurations allow simultaneously measuring the macroscopic rheology and visualizing the local droplet motions. However, the ranges of shear rates and packing fractions covered were limited by the stability of materials, which were insufficient to perform universal scaling analysis. A detailed discussion is presented in Section 2.4.

1.2. Research objectives

Previous two-dimensional experiments were performed on liquid foams with a confined plate on top to improve the material stability, introducing an additional drag on the system and hampering the rheometrical measurements. Instead, a monolayer of emulsion raft was generated in our research, which was proven to be stable enough for the measurement. Flow properties of two-dimensional emulsions can be measured by interfacial rheological technique. One main challenge for interfacial rheological measurement is distinguishing between interfacial and bulk contributions. Various set-ups such as biconical bobs, magnetic rods, and the double wall ring (DWR, [20]) have been proposed to determine the interfacial properties. This thesis used a cylindrical Couette ring modified from DWR to measure the steady flow properties of bidisperse O/W emulsion monolayers.

In this thesis, we aim to

1. Design a cylindrical Couette ring configuration that can contain sufficient emulsion droplets, facilitate capturing droplet trajectories through the camera, and allow a wide range of shear rates and volume fractions.
2. Measure the steady flow properties of emulsion monolayers at various volume fractions by sweeping the shear stress and shear rate over several decades.
3. Perform image analysis to obtain the steady flow velocity profile and investigate the emulsion monolayers' local rheology.
4. Fit the macroscopic and local rheometrical data to a possible constitutive model and inspect whether flow curves could be rescaled onto master curves.

2

Background

2.1. Rheology

The term “Rheology” was invented by Professor Bingham of Lafayette College, Indiana. It means *the study of the deformation and flow of matter*, where *rhei* is Greek for “to stream.” This section presents an overview of basic rheology.

2.1.1. Viscosity

Given a steady shear flow, Isaac Newton hypothesized that the shear stress σ is proportional to the shear rate (velocity gradient) $\dot{\gamma}$, i.e.

$$\sigma = \eta \dot{\gamma}. \quad (2.1)$$

The constant of proportionality η is called (dynamic) viscosity, which measures fluid resistance to flow. The viscosity is constant for common flows like glycerine and water that obey Newton’s postulate. However, for many other fluids, η is a function of the shear rate $\dot{\gamma}$ and are therefore called *non-Newtonian*. In most non-Newtonian fluids, the viscosity decreases with increased shear rate, which is distinguished as *shear thinning* behavior. On the contrary, *shear thickening* fluids experience an increasing viscosity with shear rate, see Figure 2.1(a).

A sketch of the flow curve of a shear thinning material is shown in Figure 2.1(b). The black curve indicates that in the limit of very low shear rates, the viscosity is a constant, while in the limit of high shear rates, the viscosity is again a substantially smaller constant. The asymptotic viscosity values at very low and high shear rates are denoted as η_0 and η_∞ , respectively. The Cross equation [22] is commonly used to describe the shear-thinning material as

$$\frac{\eta - \eta_\infty}{\eta_0 - \eta_\infty} = \frac{1}{1 + (K_1 \dot{\gamma})^m}, \quad (2.2)$$

where K_1 is a constant parameter with the dimension of time and m is dimensionless. Another two common models are the Power law and Sisko models; both are simplified from the Cross equation by making certain assumptions. The power law model is applicable for the case $\eta \ll \eta_0$ and $\eta \gg \eta_\infty$, where the Cross equation is reduced to

$$\eta = K_2 \dot{\gamma}^{n-1}, \quad (2.3)$$

with $K_2 = \eta_0 / K_1^m$ and $n = 1 - m$. Further, if $\eta \ll \eta_0$, we have

$$\eta = \eta_\infty + K_2 \dot{\gamma}^{n-1}, \quad (2.4)$$

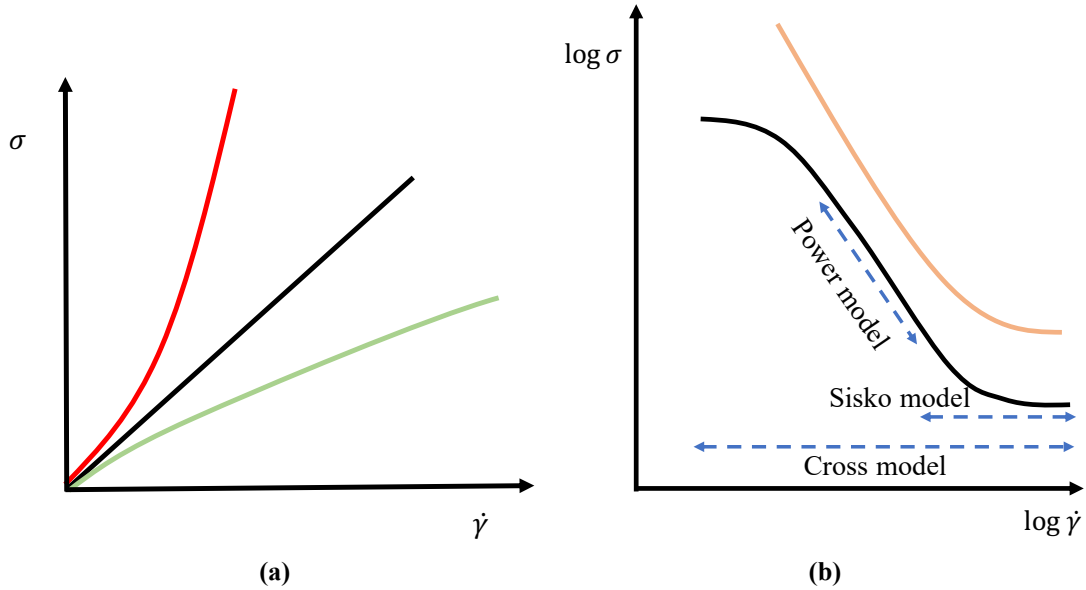


Figure 2.1: (a) Flow curves $\sigma(\dot{\gamma})$ of a shear thinning (green), Newtonian (black), and shear thickening (red) fluid. (b) Typical behavior of a shear thinning liquid with zero shear viscosity (black) and yield stress (orange) (Figure reproduced from [21]).

which is called the Sisko model [23]. The benefits of adopting such equations are that it is possible to describe the shape and curvature of a flow curve through a relatively small number of fitting parameters and to predict behavior at unmeasured shear rates [21].

In addition, some materials respond elastically to small applied stress but flow once threshold stress is exceeded. This threshold stress is called the *yield stress* (σ_y), and these types of materials are *yield stress materials*. The emulsion is one classical yield stress material: for volume fraction ϕ higher than the critical one, ϕ_c , yield stress emerges. The most commonly used model for describing yield stress materials is the Herschel-Bulkley model [24], which presupposes well-defined yield stress:

$$\sigma = \sigma_y + K\dot{\gamma}^\beta, \quad (2.5)$$

where K is called the consistency and both K and β are adjustable model parameters. After the yield stress is overcome, $\beta = 1$ refers to Newtonian fluid; $\beta < 1$ indicates fluids have shear thinning behavior; $\beta > 1$ is fluids with shear thickening behavior.

2.1.2. Viscoelastic

About ten years before Newton, Robert Hooke developed the well-known True Theory of Elasticity that for an elastic medium, the shear stress and shear strain γ are related through:

$$\sigma = G\gamma, \quad (2.6)$$

with G the shear modulus.

Many materials show behavior somewhere between a viscous liquid and an elastic solid and are therefore called *viscoelastic*. A simple method of describing viscoelastic is the mechanical models, where elastic deformation is represented by a spring with stiffness G and viscous response by a dashpot, characterized by η . One straightforward model is the Maxwell model, which results

from a serial combination of the spring and the dashpot (with the same σ). Therefore, the total strain is the sum of the strains on the dashpot and spring, i.e.,

$$\gamma = \frac{\sigma}{G} + \frac{\sigma}{\eta} \cdot t. \quad (2.7)$$

Another simple model is the Kelvin model, with the spring and the dashpot placed in parallel (with the same γ) and the resulting total stress is

$$\sigma = G\gamma + \eta\dot{\gamma}. \quad (2.8)$$

2.1.3. Rheological measurement

The flow properties of fluids can be determined using rheological measurements, which are performed using rheometers. Rheometers are apparatuses that either apply a torque along the axis of a free-rotating rod and measure the resulting angular motion, or regulate the angular motion and measure the resulting torque. Depending on the measuring geometry, torque and angular displacement can be converted into shear stress and shear rate, respectively [25]. Figure 2.2 depicts three normally used measurement geometries:

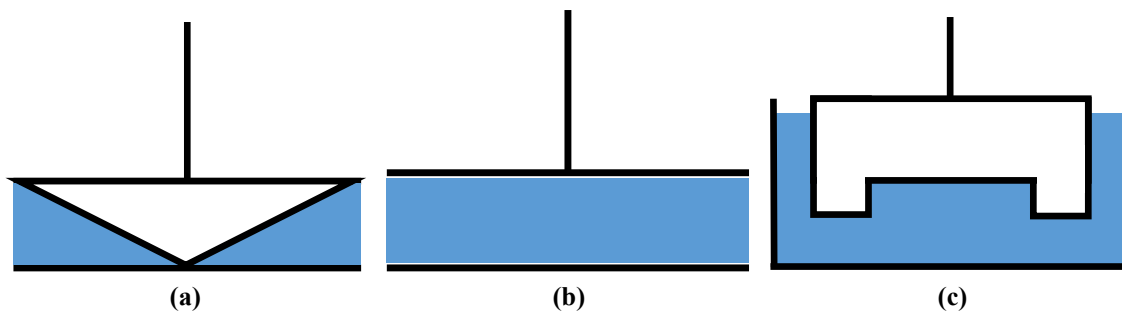


Figure 2.2: Measuring geometries: (a) cone-plate, (b) plate-plate and (c) Couette.

1. Cone-plate geometry. The gap between cone and plate increases linearly with radius, resulting in a *homogeneous* shear rate.
2. Plate-plate geometry. The top plate is rotated to shear the fluid and the shear rate increase linearly with the radius at a constant angular velocity.
3. Couette geometry. To reach a homogeneous shear stress, the inner wall's radius needs to be close to the outer wall.

A common method to determine the yield stress is *steady shear measurements*, where shear stress and shear rates sweeps are performed. The former determines the shear rate while applying shear stress within a certain range, while the latter varies the shear rates within a particular range. By fitting flow curves, i.e., shear stress as a function of the shear rate, to a rheological model, the value extrapolated to zero shear rate is the yield stress. However, the accuracy of different models when determining the yield stress depends on the lowest-measured shear rate used for the extrapolation [26].

2.2. Emulsion

Emulsions are thermodynamically unstable due to the dispersed system's large positive interfacial free energy, which decreases with the reduction of the interfacial area. The emulsion structure evolves with time due to drainage, flocculation, coalescence, and Ostwald ripening [27]. Drainage is essentially governed by the density difference between the two liquid phases, leading to a downward flow. Flocculation refers to the formation of droplet aggregates caused by depletion attractions. Coalescence is the merging of two droplets resulting from the liquid film rupture between them. Because the capillary pressure in the small droplet is higher than in the larger droplets, a mass transfer from small to big droplets happens, called Ostwald ripening.

The flow properties of emulsions are influenced by several factors, such as the viscosity of the liquids, type and concentration of the emulsifier, size distribution of the droplets, and temperature. A parameter of paramount importance is the droplet concentration, normally called volume fraction ϕ , given by the ratio of the dispersed phase's volume to the emulsion's total volume. When ϕ is higher than a critical value ϕ_c , the dispersed droplets are no longer spherical, and the system is *jammed*. An emulsion consisting of the same-sized droplets is called a monodisperse emulsion. The critical volume fraction ϕ_c equals to $\frac{\pi}{2\sqrt{3}} \approx 0.9069$ for two-dimensional monodisperse emulsions. However, as the droplet size variation (polydispersity) increases, a disordered emulsion forms, with a lower critical volume fraction, around 0.84. In three dimension, a monodisperse emulsion jams at $\phi_c = \frac{\pi}{3\sqrt{2}}$ and a polydisperse one at $\phi_c \approx 0.64$.

Several kinds of force coexist to various degrees in flowing emulsions. Firstly, there are repulsive or attractive forces between particles. For instance, The former can arise from electrostatic charges or surfactant material adsorbed on the droplet surfaces. The latter can arise from the Van der Waals attraction. Secondly, the Brownian (thermal) forces triggered by thermal fluctuations may affect the movement of droplets. In this thesis, however, emulsions are large ($\sim 2\text{mm}$) enough to neglect the Brownian force. Thirdly, the viscous forces acting on the droplets need to be considered, which are proportional to the local velocity difference between the droplets and the surrounding fluid. Hence the emulsion viscosity is usually considered as the viscosity relative to that of the continuous phase. For dilute dispersed emulsion, Einstein [28] showed that single particles increased the viscosity of a liquid as a simple function of their volume fraction:

$$\eta = \eta_s(1 + b_0\phi), \quad (2.9)$$

where b_0 is an adjustable parameter, η is the viscosity of emulsion and η_s is the viscosity of the solution. For concentrated Newtonian emulsions, the Krieger-Dougherty [29] equation is commonly used to describe the emulsion viscosity,

$$\eta = \eta_s(1 - \phi/\phi_c)^{-m}, \quad (2.10)$$

again m is an adjustable parameter. Furthermore, for the binary mixture, the Krieger-Dougherty equation becomes [30]

$$\eta = \eta_s(1 - \phi_1/\phi_{c1})^{-m_1}(1 - \phi_2/\phi_{c2})^{-m_2}. \quad (2.11)$$

2.3. Universal scaling analysis

Generally, Complex fluids are dispersions of one substance in a continuous phase, such as emulsions, foams and polymers. These materials play an essential role in industrial processes and prod-

ucts [3], and understanding and predicting the flow behavior of complex fluids is of remarkable fundamental and practical importance [31]. Despite the significant differences in physicochemical properties and length scales between the complex fluids, these materials exhibit surprisingly similar rheological properties, of which volume fraction ϕ is an important parameter.

Rheometrical measurements of complex fluids usually yield several flow curves, each corresponding to a certain volume fraction. For instance, Nordstrom et al. [9] and Paredes et al. [10] measured the rheology of colloidal gel particles and emulsions respectively, see Figure 2.3. When $\phi > \phi_c$, complex fluids will not flow but deform elastically under small stresses unless the yield stress is exceeded, whereas systems with $\phi < \phi_c$ show Newtonian behavior at low shear rates. When shear rates increase, shear thinning behavior gradually emerges for both $\phi > \phi_c$ and $\phi < \phi_c$.

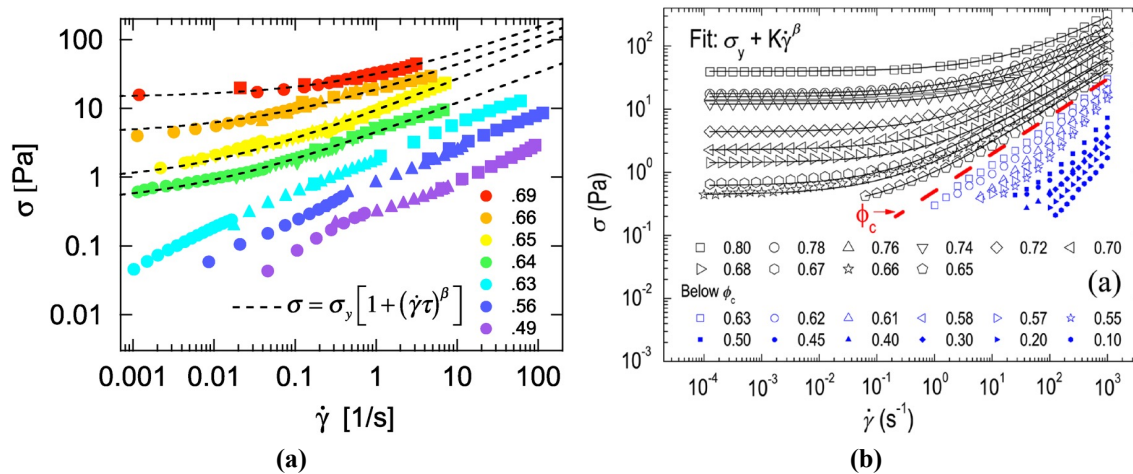


Figure 2.3: Shear stress versus strain rate given several different volume fractions (a) for colloidal gel particles (Figure reproduced from [9]). The fluid is driven through the microfluidic channel by the pressure gradient. The dashed lines are fit to the Herschel-Bulkley model, while the subcritical cases exhibit no yield stress and reduce approximately to a power law. (b) for castor oil emulsion sheared in a cone-plate geometry. The solid lines represent the Herschel-Bulkley fit and in the subcritical branches are the Cross fit. Black symbols and blue symbols correspond to samples with $\phi > \phi_c$ and $\phi < \phi_c$ respectively. (Figure reproduced from [10])

Furthermore, Nordstrom et al. and Paredes et al. respectively scaled the log-log flow curves on two branches, see Figure 2.4: at low shear rates, the supercritical master curve approaches a constant, which corresponds to the existence of the yield stress for a jammed system, whereas the subcritical master curve is close to a straight line with a unit slope, as will be shown later, which confirms the Newtonian behavior for $\phi < \phi_c$ system. On the other hand, both two curves exhibit shear thinning behavior, with slopes smaller than one at high shear rates. Two exponents, Δ and Γ , need to be extrapolated from data fitting, and experiments for different complex systems provided similar values (see Table 2.1), with $\Delta \approx 2$ and $\Gamma \approx 4$. One implicit parameter, the critical volume fraction ϕ_c , is also extrapolated from scaling analysis since it is nontrivial to reach the jamming point with high precision in experiments. Consequently, researchers are equally keen to explore the rheological behavior of complex fluids by numerical simulations, which can approach the jamming point much more closely.

The scaling exponents predicted by different experiments and simulations are summarized in Table 2.1. Whereas experimental research on the flow curves of yield-stress materials gave similar

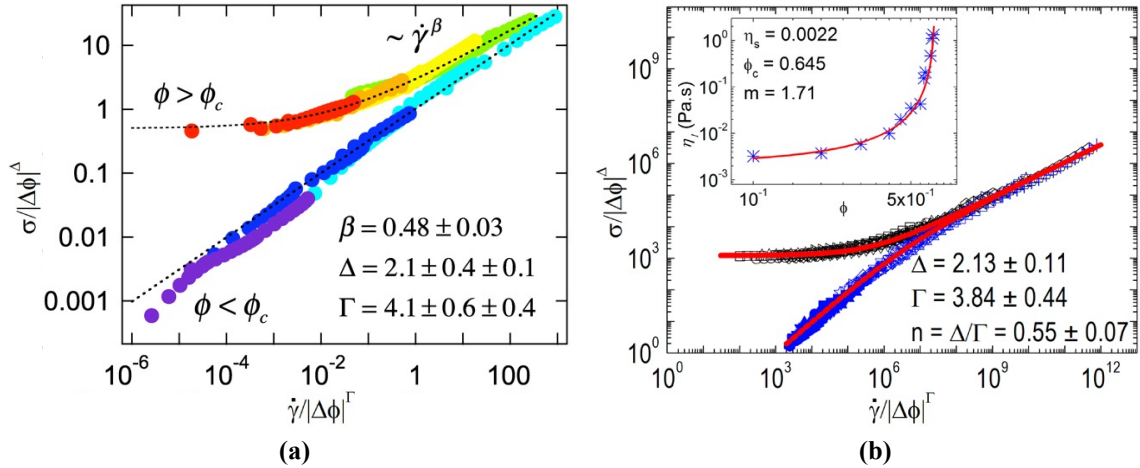


Figure 2.4: Master curve showing collapse of flow curves, one for samples with $\phi > \phi_c$ and one for samples with $\phi < \phi_c$ when plotted as $\sigma/|\Delta\phi|^\Delta$ versus $\dot{\gamma}/|\Delta\phi|^\Gamma$ (a) for colloidal gel particles (Figure reproduced from [9]). The first exponent uncertainties are statistical; the second are systematic. (b) for castor oil emulsion sheared in a cone-plate geometry. Inset: Fit of the Newtonian viscosity to the Krieger-Dougherty equation, giving $\eta_s = 2.2 \times 10^{-3} \text{ Pa} \cdot \text{s}$ and $m = 1.71$ with $\phi_c = 0.645$. (Figure reproduced from [10])

scaling parameters for soft sphere systems with different interparticle interactions, numerical estimates of the scaling exponents were different from experiments. Dekker et al. [16] investigated the discrepancy between simulations and experiments and gave two possible explanations: the models used in simulations describe different material properties from experimental subjects and the response window for two methodologies are different as simulations are able to approach the jamming point much closer than in experiments and hence focus on situations where the accuracy of experimental measurements is not achievable.

It is evident from the Table 2.1 that the experimental studies so far have not ventured into universal scaling analysis for two-dimensional complex fluids. Although some two-dimensional experiments have been performed to study the rheological behavior of such materials, as will be reviewed in Section 2.4, none gave universal scaling of flow curves, partly due to the limitations of material stability. The potential and advantages of two-dimensional research are embodied in the following aspects. Firstly, two-dimensional configurations allows simultaneously tracking the position of all droplets (bubbles) and measuring rheological properties. While the rheometer measures the global behavior of the complex fluid, the velocity profile produced from droplet (bubble) trajectories allows the analysis of the behavior at a droplet (bubble) scale. Due to the discrete nature of complex fluids, constructing a plausible connection between local and global behaviors can provide more insight. Secondly, the previous two-dimensional experiments failed to systematically distinguish the bulk flow contribution from the interfacial measurements. Only in a small range of shear rates did investigators confirm a negligible drag contribution from bulk flow, limiting the range of shear rates for measurements. As described in Section 2.5, the effect of bulk flow on the measurement can be inhibited to a negligible degree by choosing a suitable experimental geometry, and therefore the behavior of the monolayer substance dominates in the measurement. Additionally, scaling exponents predicted by two-dimensional experiments can serve as a reference for the 2D simulations. While numerous scaling exponents characterizing geometry and mechanics are found to be the same in 2D and 3D [36], 2D simulations are of preference since they are (comparatively) computationally inexpensive.

Literature	Systems	Methods	Yield stress Δ	Shear rate Γ	Shear thinning β	Critical volume fraction ϕ_c
K.N. Nordstrom, et al. [9]	Monodisperse hydrogel particles, microfluid channel		$2.2 \pm 0.4 \pm 0.1$	$4.1 \pm 0.6 \pm 0.4$	0.48 ± 0.03	0.635 ± 0.003
J. Paredes, et al. [10]	Monodisperse mobile emulsion, cone-plate	3D experiment	2.13 ± 0.11	3.84 ± 0.44	0.55 ± 0.07	0.645 ± 0.005
A.Basu, et al. [11]	Monodisperse hydrogel particles, cone-plate		2.6 ± 0.7	5.0 ± 1.0	0.52 ± 0.16	0.61 ± 0.03
	Bidisperse hydrogel particles, cone-plate		2.6 ± 0.8	5.6 ± 1.0	0.46 ± 0.17	0.61 ± 0.03
M. Dinkgreve, et al. [12]	Monodisperse rigid emulsion, cone-plate		2.04 ± 0.13	3.80 ± 0.34	0.54 ± 0.06	0.64 ± 0.06
	Monodisperse aqueous foam		2.21 ± 0.21	3.75 ± 0.20	0.59 ± 0.07	0.68 ± 0.03
R.I. Dekker, et al. [16]	Monodisperse mobile emulsion, cone-plate		2.13 ± 0.15	3.84 ± 0.59	0.56 ± 0.05	0.64
P.Olsson, et al. [13]	Bidisperse frictionless disks, harmonic repulsion	2D simulation	1.2	2.85	0.42	0.8415
T.Hatano, et al. [32]	Bidisperse frictionless particles, Hertzian interaction	3D simulation	1.8 ± 0.1	2.4 ± 0.1	0.75	0.6415 ± 0.0065
	Bidisperse frictionless particles, harmonic interaction		1.2 ± 0.1	1.9 ± 0.1	0.63	
B.P.Tighe, et al. [14]	Bidisperse frictionless disks, harmonic interaction	2D simulation & model	2	4	0.5	0.8423
M.Otsuki, et al. [33]	Bidisperse frictionless disks, harmonic interaction	3D simulation	1	2.5	0.4	0.648
	Polydisperse frictionless disks, Hertzian interaction	2-4D simulation				$D = 2, 0.8438$
			1.5	2.75	0.54	$D = 3, 0.6446$
						$D = 4, 0.4614$

Table 2.1: Scaling exponents collected from experiments and simulations for systems with various interparticle interactions. All experiments are three-dimensional and give similar predictions, $\Delta \approx 2$, $\Gamma \approx 4$, $\beta \approx 0.5$ and $\phi_c \approx 0.64$. Nevertheless, numerical simulations with different interparticle interactions and dimensions give various predictions for exponents. Note that the most “classic” mixture of bidisperse packings is that large and small disks with a 1.4:1 ratio of their radii are mixed in equal amounts [34]. The elastic forces between particles are modeled as “one-sided springs”: $f_{el} \sim \delta_{el}^\alpha$, where δ is the dimensionless compression of the spring and $\alpha = 1(3/2)$ corresponds to harmonic (Hertzian) forces [35].

2.3.1. Methodology of universal scaling analysis on flow curves

This section summarizes a framework of universal scaling analysis for complex fluid flow curves. Most of this section is adapted from Paredes et al. [10], which could be a viable choice for subsequent data fitting.

Empirical equations are usually adopted to describe the generic behavior of complex fluids, which can fit the flow curves with a few parameters. For instance, the flow behavior of the concentrated systems above the jamming point is often successfully described by the Herschel-Bulkley equa-

tion (Equation 2.5), with $\beta < 1$ describing the shear thinning behavior. The Herschel-Bulkley model has a built-in yield stress which equals zero at the jamming point. Consequently, the vanishing of the yield stress with decreasing volume fraction is usually described as a power law in the distance to the jamming:

$$\sigma_y = \sigma_0 |\Delta\phi|^\Delta, \quad (2.12)$$

with $\Delta\phi = \phi - \phi_c$. Below ϕ_c , it has been reported [10] that the generically observed Newtonian-to-shear-thinning behavior with increasing shear rate can be well described by a Cross-type equation:

$$\sigma = \frac{\eta_N \dot{\gamma}}{1 + C \dot{\gamma}^{1-\delta}}, \quad (2.13)$$

where C and δ ($0 < \delta < 1$) are adjustable parameters. The Newtonian viscosity η_N is evaluated from the Krieger-Dougherty equation (Equation 2.10). An equivalent power law expression is

$$\eta_N = \eta_0 |\Delta\phi|^{-m}, \quad \eta_0 = \eta_s \phi_c^m. \quad (2.14)$$

As shown in Figure 2.4, flow curves with respect to the volume fraction can be scaled into two master curves, one for the supercritical and one for the subcritical volume fractions, by plotting $\sigma/|\Delta\phi|^\Delta$ versus $\dot{\gamma}/|\Delta\phi|^\Gamma$. Relations between parameters ($\Delta, \Gamma, \beta, \delta, K, m$) in Paredes's framework could be derived by considering two limiting cases: $\dot{\gamma} \rightarrow 0$ and $\dot{\gamma} \rightarrow \infty$.

$$\text{Case 1: } \dot{\gamma} \rightarrow 0, \quad \left. \begin{aligned} \sigma &= \sigma_y + K\gamma^\beta && \approx \sigma_y, && \phi > \phi_c, \\ \sigma &= \eta_N \dot{\gamma} / (1 + C\dot{\gamma}^{1-\delta}) && \approx \eta_N \dot{\gamma}, && \phi < \phi_c. \end{aligned} \right\} \quad (2.15)$$

$$\text{Case 2: } \dot{\gamma} \rightarrow \infty, \quad \left. \begin{aligned} \sigma &= \sigma_y + K\gamma^\beta && \approx K\dot{\gamma}^\beta, && \phi > \phi_c, \\ \sigma &= \eta_N \dot{\gamma} / (1 + C\dot{\gamma}^{1-\delta}) && \approx \frac{\eta_N}{C} \dot{\gamma}^\delta, && \phi < \phi_c. \end{aligned} \right\} \quad (2.16)$$

At high strain rates, both supercritical and subcritical master curves approach an asymptotic line $\log_{10}(\sigma/|\Delta\phi|^\Delta) = k_1 \log_{10}(\dot{\gamma}/|\Delta\phi|^\Gamma) + b_1$, which gives

$$\left. \begin{aligned} \phi > \phi_c, & \quad \frac{K\dot{\gamma}^\beta}{|\Delta\phi|^\Delta} = 10^{b_1} \left(\frac{\dot{\gamma}}{|\Delta\phi|^\Gamma} \right)^{k_1} \\ \phi < \phi_c, & \quad \frac{\frac{\eta_N}{C}\dot{\gamma}^\delta}{|\Delta\phi|^\Delta} = 10^{b_1} \left(\frac{\dot{\gamma}}{|\Delta\phi|^\Gamma} \right)^{k_1} \end{aligned} \right\} \Rightarrow \beta = \delta = \frac{\Delta}{\Gamma} = k_1, \quad K = \frac{\eta_N}{C} = 10^{b_1}. \quad (2.17)$$

On the other hand, at very low strain rates, the master curve for $\phi < \phi_c$ approach to another asymptote $\log_{10}(\sigma/|\Delta\phi|^\Delta) = k_2 \log_{10}(\dot{\gamma}/|\Delta\phi|^\Gamma) + b_2$, while the other curve is close to a constant b_3 :

$$\left. \begin{aligned} \phi > \phi_c, & \quad \frac{\sigma_y}{|\Delta\phi|^\Delta} = 10^{b_3} \\ \phi < \phi_c, & \quad \frac{\eta_N \dot{\gamma}}{|\Delta\phi|^\Delta} = 10^{b_2} \left(\frac{\dot{\gamma}}{|\Delta\phi|^\Gamma} \right)^{k_2} \end{aligned} \right\} \Rightarrow \sigma_0 = 10^{b_3}, \quad k_2 = 1, \quad \eta_0 = 10^{b_2}, \quad m = \Gamma - \Delta. \quad (2.18)$$

An extra implicit variable, the critical volume fraction ϕ_c is determined from Equation 2.12 by

extrapolating the yield stress to zero.

2.4. Two dimensional experiments on complex fluids

In the following chapter, we will describe experiments on the rheology of monolayer emulsions (i.e., two-dimensional emulsions). Hence, this section will first review the relevant literature on the rheological behavior of similar two-dimensional complex fluids. To be precise, all the experimental subjects in the reviewed literature are millimeter-sized two-dimensional liquid foams due to their similar length scales and rheological properties to the emulsions used in the present work.

For two-dimensional foams, three experimental configurations have been studied in the literature with different boundary conditions: the Hele-Shaw cell, where bubbles are confined between two glass plates [37], the bubble raft, where a monolayer of bubbles float freely at the surface of the solution [38], and the confined bubble raft, where bubbles are confined between the surface of the solution below and a glass plate on top [39]. It was found that confining bubbles with a top plate significantly improved the stability of the foam [40], i.e., the foam rarely ruptured or coalesced within experimental time scale and the confining plates served to suppress the vertical deformation of the bubbles. However, there is still no consensus on what effect glass plates will have on the rheology of two-dimensional foams. For instance, Debrégeas, Tabuteau, and Di

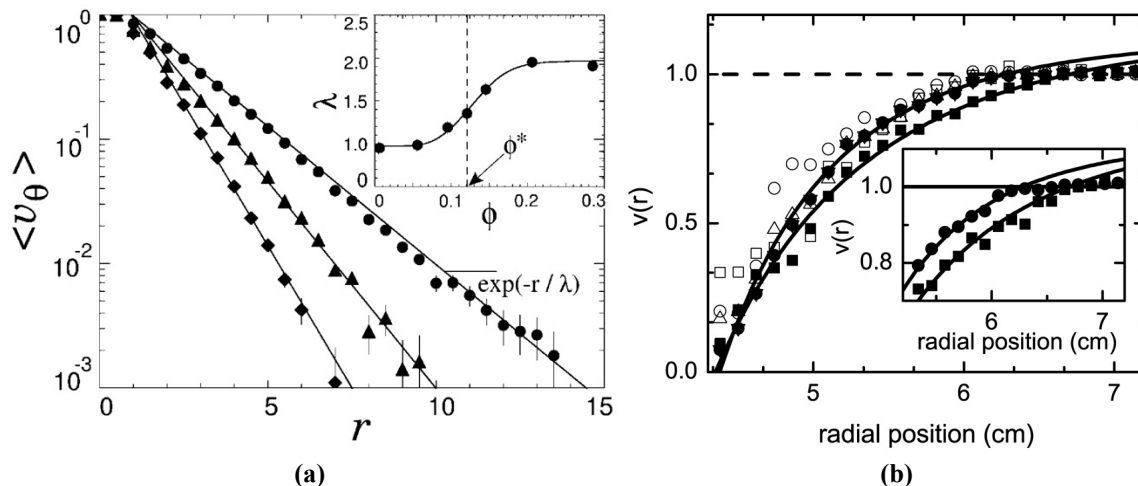


Figure 2.5: Velocity profiles (a) for bidisperse foam confined in a Hele-Shaw geometry with inner wall rotating (\bullet : $\phi = 0.80$; \blacktriangle : $\phi = 0.88$; \blacklozenge : $\phi = 0.95$). Note that it's a log scale plot and the small plateau for $0 < r < 1$ corresponds to first row of bubbles, not shear rate discontinuity. (Figure reproduced from [37]) (b) for bidisperse bubble raft in a cylindrical Couette configuration with outer wall rotating at $\Omega = 5 \times 10^{-3}$ rad/s (\bullet) and $\Omega = 8 \times 10^{-3}$ rad/s (\blacksquare). The inset shows a close look at the discontinuity of shear rates. (Figure reproduced from [17])

Meglio [37] sheared a bidisperse foam in a Hele-Shaw cell with a cylindrical Couette geometry and to reduce the effect of the viscous friction between the bubbles and the confining plates, they restricted their study to quasistatic flows, where bubbles were sheared at sufficiently low strain rates and “the associated timescale is slower than kinematic relaxation times”. The measured average azimuthal velocity profiles were shown to be independent of the shear rate within a range of driving velocities, supporting their quasistatic assumption because changes in velocity differences should result in different magnitudes of friction. In addition, the velocity profile exhibiting a rapid exponential decay to zero over a few bubble diameters is the so-called *shear*

localization behavior, see Figure 2.5 (a), and this localization of velocity becomes closer to the driving wall as the liquid fraction ($\phi_l = 1 - \phi$) decreases.

The nature of exponential decay reported by Debrégeas et al. implies a continuous strain rate, but this is contrary to the conclusions from Lauridsen et al. [41, 17], where the authors sheared a polydisperse bubble raft in a cylindrical Couette geometry at low strain rates and showed a non-smooth averaged velocity profile, suggesting the shear rate is discontinuous in the radius direction. The velocity data were then fitted with a power-law model for viscosity (Equation 2.3), which gives a good fit between the inner wall r_i and a critical radius r_c but fails after that, where the shear rate discontinuity starts (the solid lines in Figure 2.5(b)). This discontinuity is called *shear banding*. It should be noted that in Lauridsen and his colleagues' experiments, the outer cylinder was rotated, and hence the existence of r_c implied that a portion of the bubble raft followed the outer cylinder wall as if it were a solid. In addition, this critical radius was seen to be dependent on the driving velocity, which contradicts the rate independence at low shear rates claimed by Debrégeas et al. [37]. Gilbreth et al. [42] observed a similar shear banding for the bubble raft, which exhibits the coexistence of a power-law fluid and a rigid body, with a discontinuity in the shear rate. The following constitutive equation first stemmed from three-dimensional experiments on emulsions [43] and foams [44], could be used to describe the coexistence of flowing and solid-like regions:

$$\begin{aligned} \dot{\gamma} &= 0 && \text{for } \dot{\gamma} < \dot{\gamma}_c, \\ \sigma &= \mu(\dot{\gamma}/\dot{\gamma}_c)^n, && \text{for } \dot{\gamma} > \dot{\gamma}_c, \end{aligned} \quad (2.19)$$

where $\dot{\gamma}_c$ refers to the non-zero limit of $\dot{\gamma}$ at r_c . Another model, Herschel-Bulkley equation mentioned before, has a built-in yield stress and hence describes the transition from fluid-like to solid-like behavior as well. However, this model is explicitly continuous in the shear rate and fails to predict the discontinuity of shear rates at r_c [42].

One may attribute differences in the velocity profiles in the Hele-Shaw cell and the bubble raft, i.e., whether the shear rate is continuous and whether the velocity profile is independent of the shear rate, to the existence of the confining plates. Interestingly, Katgert et al. [40] came to a completely different conclusion from Debrégeas et al. and Lauridsen et al. Although, again, bidisperse bubbles are sheared in the two-dimensional cylindrical Couette geometry, his results showed that the velocity profiles with top plate exhibit rate dependence, whereas the velocity profile for bubble rafts are approximately $\dot{\gamma}$ independent, see Figure 2.6. Continuous transitions in the shear rate and shear localization were observed in both cases. However, the shear localized velocity profile for the bubble raft is due to the fact that stresses decay as $1/r^2$ in the Couette geometry, as we will see later, while for bubbles with a top plate, the much stronger rate-dependent shear localization is the result of both geometry's curvature and the difference in magnitude between bubble-bubble drag and bubble-plate drag. Note that at higher driving velocity, the velocity profile has a wider localized region.

Instead of cylindrical Couette geometry, Wang et al. [18] investigated the role of the confining plate in a plane-Couette geometry, where monolayers of monodisperse bubbles were sheared linearly by two counter-propagating belts at low shear rates. If the quasistatic assumption is viable, the velocity profiles should be similar for different boundary conditions; however, as shown in Figure 2.7, the velocity profile exhibits rate independence both with and without a top plate, but the shapes are rather distinct. The velocity profile of the bubble raft is close to a straight line, resembling the continuous steady flow between two parallel plates. However, the

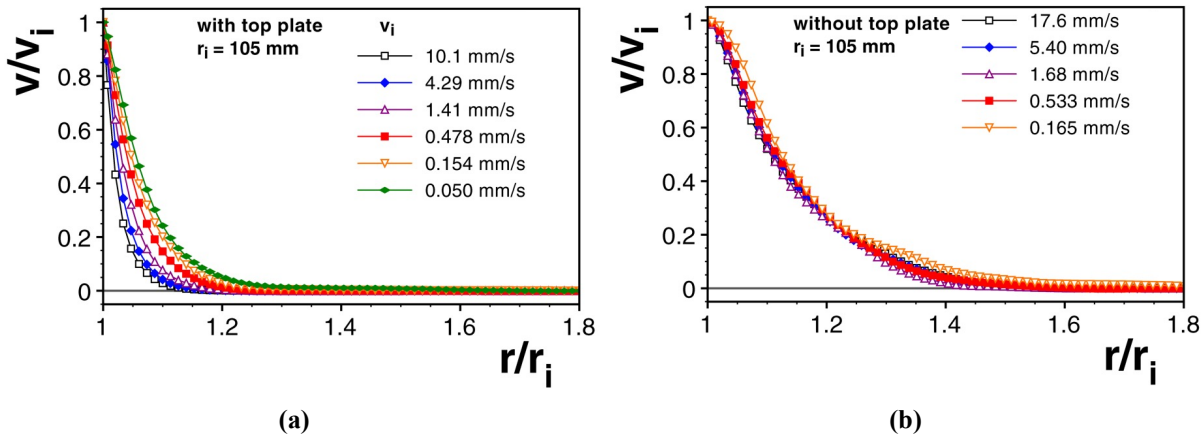


Figure 2.6: Velocity profiles for the bidisperse foam sheared in a Taylor-Couette geometry (a) with top plate: the curves exhibit strong shear banding and rate-dependence. (b) without top plate: the curves are approximately rate-independent velocity profiles and the shear banding is due to the curved geometry (Figures reproduced from [40]).

confined bubble flow shows shear localization, where the velocity decays exponentially. The difference between velocity profiles has evidenced the crucial role played by the confining plate and indicates that only considering the nonuniform stress imposed by the plane-Couette geometry is not sufficient to explain the formation of shear localization with exponentially decaying velocity [45], similar to the case of the cylindrical Couette geometry discussed before, see Figure 2.6.

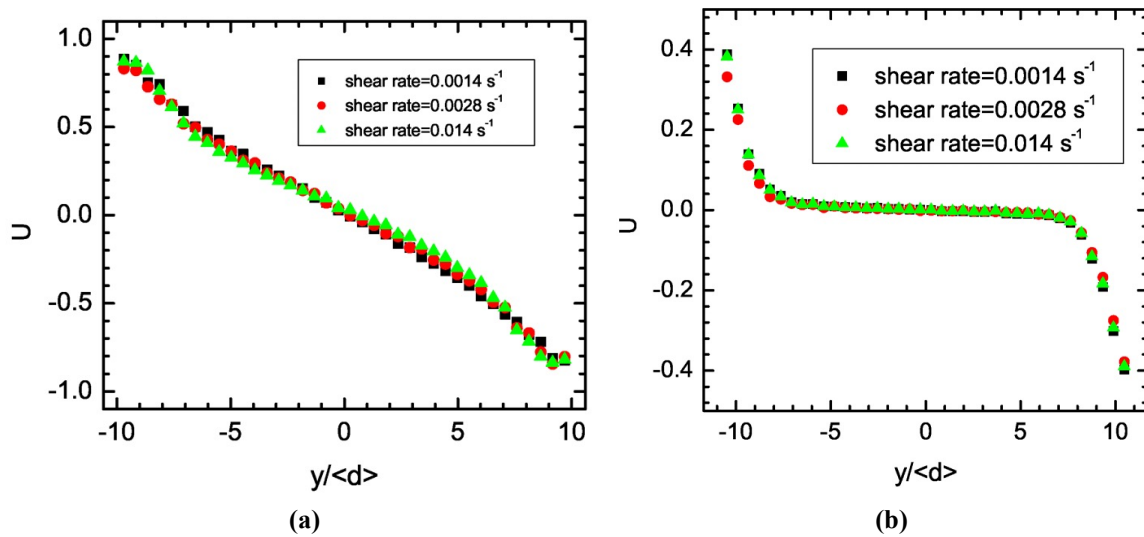


Figure 2.7: Velocity profiles for the linearly sheared *monodisperse* foams (a) without top plate: the curves are close to linear; (b) with top plate: the curves show strong shear banding behavior (Figures reproduced from [18]). Note that both cases result in rate-independent velocity profiles.

Furthermore, Katgert et al. [46] gave a comparable outcome for the confined monodisperse foam in the linear sheared geometry (Figure 2.8(a)), and they further claimed that the bidispersity of the liquid foams contributed to the rate dependence of the velocity profile (Figure 2.8(b)). By defining an averaged viscous friction between bubbles that balances the viscous friction between bubbles and top plate and scaling two types of viscous friction to velocity difference Δv , Katgert,

Tighe and Hecke [35] found that inter-bubble friction scales as $F_v \sim \Delta v^{0.67}$ for monodisperse foams and $F_v \sim \Delta v^{0.36}$ for bidisperse foams. Consequently, the rate dependence of the velocity profile is attributed to the bidispersity of the foams, which “enhances the averaged viscous dissipation inside the foam with respect to the monodisperse case”.

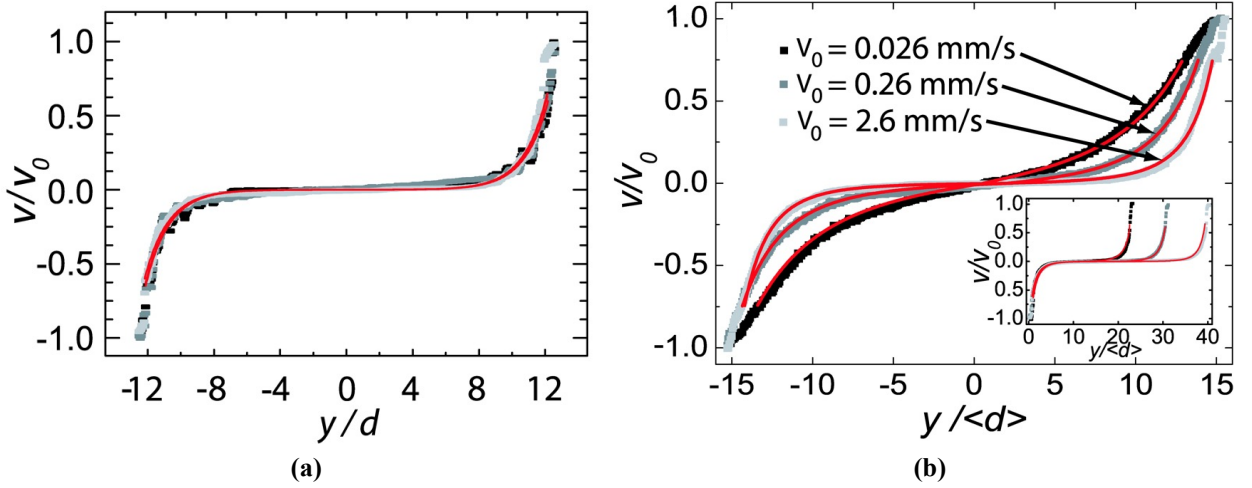


Figure 2.8: (a) Velocity profiles of the linearly sheared *monodisperse* foam with a top plate, exhibiting rate-independence for 0.083mm/s (black curve), 0.26mm/s (dark gray curve), and 0.83mm/s (light gray curve). (b) Velocity profiles for the linearly sheared *bidisperse* foam with a top plate, which is rate dependent. Figures are reproduced from [46].

To summarize, the confining plate serving to suppress the buckling of the monolayer bubbles imposes an extra bubble-wall viscous friction to the system and hence brings about the strong shear localized velocity profile, which cannot be fully explained by the nonuniform stress imposed by cylindrical Couette geometry (Figure 2.5(a), Figure 2.6(a)) and plane Couette geometry (Figure 2.7 (b)). Besides, by scaling analysis, the bidispersity is found to enhance the dissipation of the averaged inter-bubble friction, contributing to the rate dependence of velocity profiles (Figure 2.6(a), Figure 2.8(b)). However, for the monodisperse foams where the competition between bubble-bubble friction and bubble-plate friction is not comparable, the velocity profiles may remain rate-independent (Figure 2.6(b), Figure 2.8(a)). However, most two-dimensional foam experiments investigated the rheological behavior at a fixed volume fraction. Although very few have explored the effect of the packing fraction, they were performed at very low shear rates due to the quasistatic limit. Such a range of volume fractions and shear rates is insufficient to predict a universal scaling law of the two-dimensional complex fluid as in three-dimensional experiments. Yet a plausible explanation for the shear discontinuity displayed by the bubbles floating freely in the cylindrical Couette geometry is still expected; an appropriate model to fit the velocity profile should be carefully chosen once this shear banding occurs. Furthermore, all the velocity profiles shown above are both spatially and temporally averaged, neglecting the discontinuity nature of complex fluid; still, how the instantaneous movement of bubbles (droplets) affects the global measurements needs further investigation.

2.5. Experimental set-up for interfacial rheology

The rheological properties of monolayer emulsions will be determined by interfacial rheological measurements in this work. Interfacial properties can be classified as dilatation or shear, and we

will only focus on the shear behavior of emulsions. This section presents several devices and measuring probes available for interfacial rheological measurements.

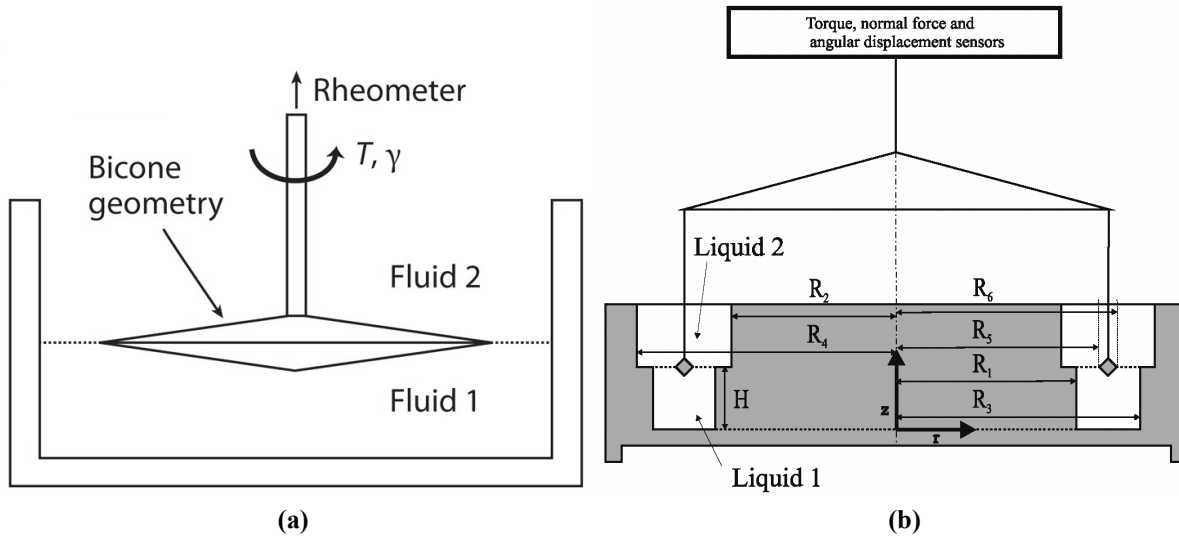


Figure 2.9: (a) Cross section of bi-cone geometry (Figure reproduced from [47]). (b) Cross section of the DWR setup (Figure reproduced from [20]).

One of the main challenges in designing an interfacial rheometer is distinguishing between the bulk and interface contributions as they both influence the surface flow behavior. The Boussinesq number (Bo) [48] is defined to describe the importance of the surface drag to the bulk as:

$$Bo = \frac{\text{surface drag}}{\text{subphase drag}} = \frac{\eta_I \cdot \frac{V}{L_I} \cdot P_I}{\eta_s \cdot \frac{V}{L_s} \cdot A_s} = \frac{\eta_I}{\eta_s \cdot G}, \quad (2.20)$$

where η_I is the surface shear viscosity (units: Pa s m), η_s is the average bulk viscosity (units: Pa S), L_I and L_s are the characteristic length scale over which the characteristic velocity V decays at the interface and in the subphase, respectively. A length scale G is defined as $\frac{A_s L_I}{P_I L_s}$ where P_I is the contact perimeter between the surface probe and the interface and A_s is the contact area. When $|Bo| \gg 1$, the contribution from the surface dominates the measurement and forces coming from the bulk owing to the velocity gradients in the surrounding fluid phases are negligible. This can be achieved by minimizing the length scale G in Equation 2.20, which is dependent only on the geometry of the measurement system. Figure 2.9 presents some common used measurement geometries. The magnetic rod rheometer [49] imposes an interfacial shear flow by placing a thin rod at the interfaces driven by a magnetic field. The simple geometry is a good design for minimizing G , but the dynamic range is limited because sufficient buoyancy and surface tension are required for the rod to float. On the other hand, bi-cone [50] geometry consisting of a disk with a small cone angle attached to a conventional rheometer can provide a large dynamic range. However, the length scale G is large due to its geometry.

The 2D equivalent of a double-wall Couette geometry is the double-wall ring (DWR) introduced by Vandebril et al. [20]. It takes advantage of certain aspects of the magnetic rod and bi-cone geometry: the length scale G is minimized, and the device can be mounted onto a conventional rheometer easily, enabling a wide dynamic range. As depicted in Figure 2.9(b), the sample is contained in a double-wall trough, and a square-shaped ring is positioned at the interface and

connected to a rheometer. Sometimes openings on the ring are designed to ensure a homogeneous surface pressure in and outside the ring. The interfacial perimeter $P_I = 2\pi(R_5 + R_6)$ and the contact area $A_s = \frac{\pi(R_6^2 - R_5^2)}{\cos(\pi/4)}$, thus the length scale G is given as

$$G = \frac{L_I}{L_s} \frac{R_6 - R_5}{\sqrt{2}}. \quad (2.21)$$

However, the flow field in DWR is ill-defined. Therefore, a Couette ring modified from DWR will be presented in the next chapter, specifically designed to measure both the macroscopic and local rheological properties of monolayer emulsions.

Experimental setup and methods

3.1. Design Targets

Our experiments were designed to measure the **steady flow curves** of emulsion monolayers, which, similar to Figure 2.3, consists of three main components, the shear stress σ , the shear rate $\dot{\gamma}$ and the volume fraction ϕ , with the shear rate derivable from the velocity profile. In a rheological measurement, well-defined flow configurations are typically implemented so that, with only geometry information and force measurement, an analytical solution exists for either the shear stress or the velocity profile, regardless of the measured material. As discussed in the previous chapter, a two-dimensional configuration facilitates the visualization of dispersed phases while simultaneously measuring the rheology, and is therefore well-suited for experimentally investigating the rheology of complex fluids. One of the main challenges in designing an interfacial rheometer is distinguishing between the bulk and interface contributions as they both influence the surface flow behavior, which can be evaluated by Boussinesq number (Equation 2.20). To summarize, three design targets should be achieved for our experiments:

- A well-defined flow field.
- An interfacial drag dominant configuration.
- A clear visualization of droplet motions and packings.

3.2. Experimental setup

The experimental setup is shown in Figure 3.1. Two needles connected with a syringe pump are inserted vertically to create droplets with two diameters. Oil droplets are blew into surfactant solution, floating between the inner ring and the cup wall. The inner ring is connected to the rheometer and shears the emulsion monolayers from the side, forming a cylindrical Couette configuration. At the bottom, the LED light sheds from the side and generates a pure white background light through the glass diffuser. On the top there is a mirror tilted at 45 degrees to increase the imaging distance from the camera. For a two-dimensional Couette configuration, the shear stress and shear rates are calculated by

$$\sigma = \frac{T}{2\pi r^2}, \quad (3.1)$$

and

$$\dot{\gamma} = \frac{v_\theta}{r} - \frac{\partial v_\theta}{\partial r}, \quad (3.2)$$

where T is the torque measured by rheometer, v_θ is the steady angular velocity, and r is the radial position. The units for interfacial shear stress is $\text{Pa} \cdot \text{m}$.

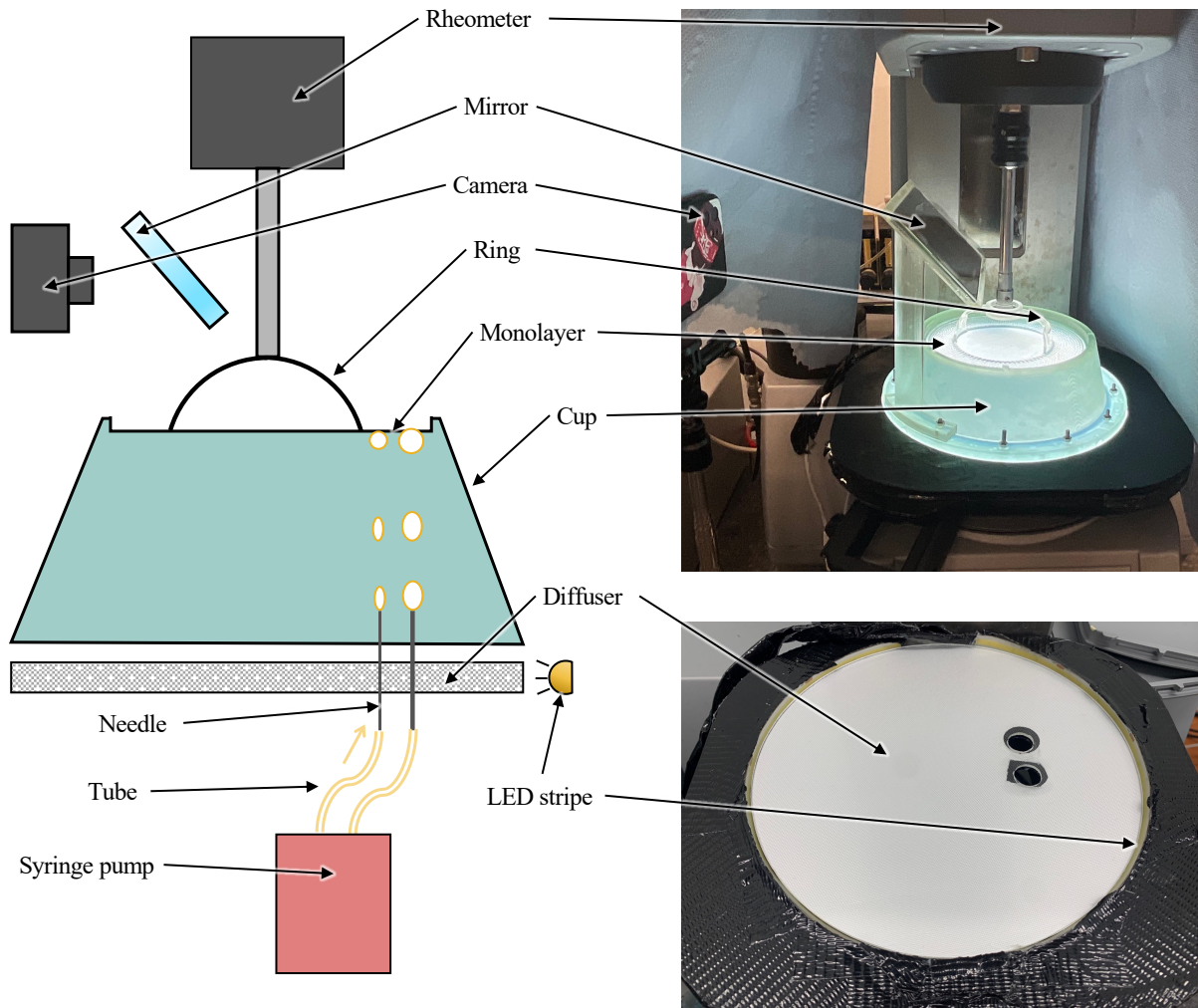


Figure 3.1: Sketch of Couette ring configuration used in this experiment.

3.2.1. Couette-ring cup

To ensure high-quality imaging, the droplet reservoir requires a transparent bottom to optimize the light transmission. Given that the 3D printing material we utilized lacked the desired transparency, a modular design was adopted, allowing for the separate manufacturing of the cup's components. The body of the cup was 3D printed using clear resin, while the mirror support and inner ring were printed with blue resin. A circular plate fashioned from a transparent acrylic sheet (4mm) serves as the cup bottom, with two small holes for the needles to pass through. Furthermore, the primary body of the cup features a slanted wall to mitigate the shadowed region arising from light refraction, see Figure 3.2(a). As depicted in Figure 3.2(b), the shadowed region emerges in a standard beaker with a vertical wall, hampering the imaging analysis.

The modular assembly with all components connected through screws facilitates the iterative design of the device but poses a challenge of waterproofing as well. A ring-shaped mould was

designed to prevent leakage, which can be filled with Polydimethylsiloxane (PDMS) material to form a waterproof ring, see the dark blue ring in Figure 3.2(c). In addition, a thin layer of Vaseline was applied at the screw mouth and the contact area between the cup's bottom and wall to further enhance the waterproofing. The cross-section of the wall and ring are square-shaped with a sharp edge to create a planar interface as much as possible. Both the inner ring and the outer wall are grooved with 2mm grooves, and the tip of grooves is defined as the wall boundary, with $R_i = 35.0$ mm and $R_o = 48.9$ mm, see Figure 3.3(b).

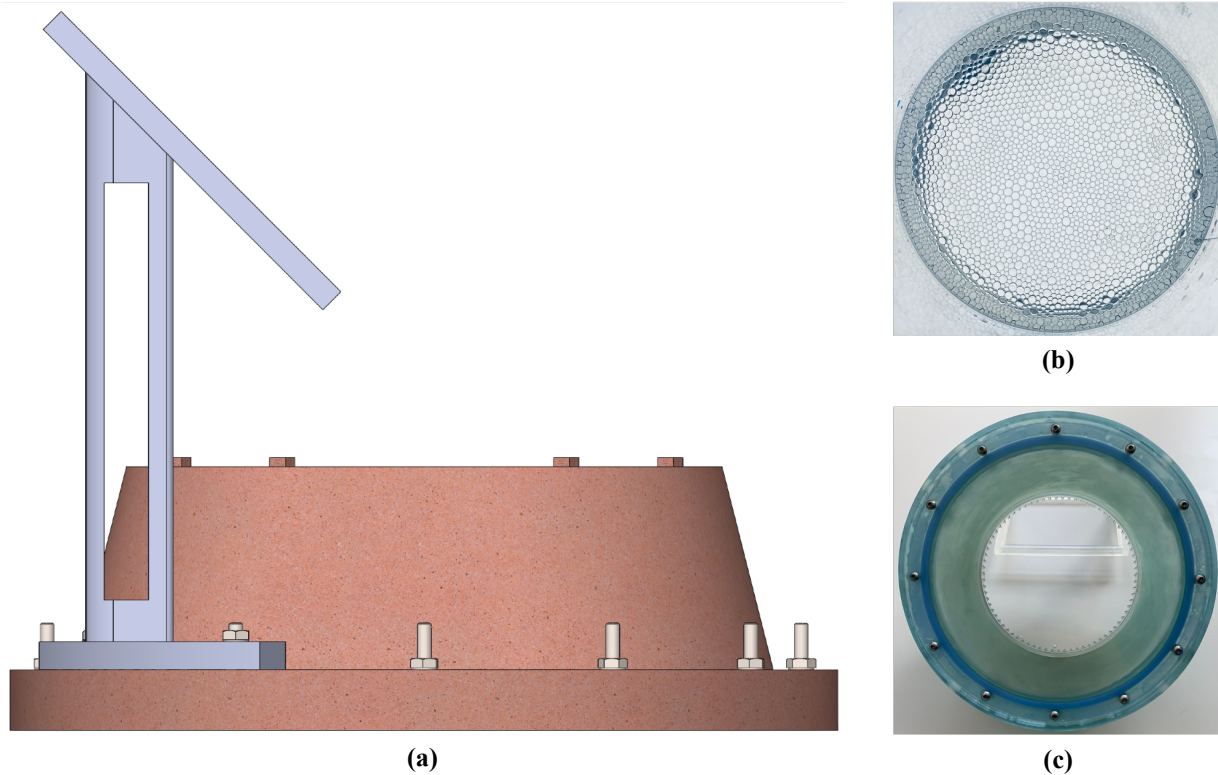


Figure 3.2: (a) A SolidWorks model of the slanted cup wall. The cup and the mirror support are connected by screws. (b) An image of the shadow region caused by light refraction in a normal beaker with a vertical wall. (c) A photo of the PDMS ring (dark blue) used to seal the gap between the 3d printed cup wall and the acrylic cup bottom.

3.2.2. Background illumination system

The background illumination system serves the dual purpose of providing uniform bright light and accommodating the connection to the rheometer, centering the cup, and simultaneously allowing the passage of needles. Figure 3.3(a) depicts the detailed structure of the backlight device, consisting of a centering ring, a diffusing paper, a glass diffuser, a reflecting paper, a LED stripe, a light container and a connector to the rheometer. A 6000K cold white LED stripe, affixed to the light container, surrounds a glass diffuser to ensure a consistent and bright light. An opaque white paper below the glass diffuser directs light upwards, while a diffusing paper above further enhances light uniformity. The component at the bottom is connected to the rheometer through three screws, with a large channel in the center to allow the passage of needles. A centering ring is adopted to bridge the gap between the light container and the cup base.

During the manufacturing process, we encountered a challenge with the dimensions of the light container exceeding the 3D printer's workspace. In addition, the limited distance from

the rheometer's side wall to the center of the cup constrained the space for the light container and LED stripe. Therefore, we changed the design from a concentric circular structure to an eccentric structure, see photos on the right in Figure 3.1. Instead of 3D printing the container and the centering ring, we manufactured them layer by layer with the laser cut technique on a 4mm acrylic plate, assembled those plate components, and sprayed them with black paste. As shown in Figure 3.2(b), the resulting design provides a bright and well-centered background illumination system.

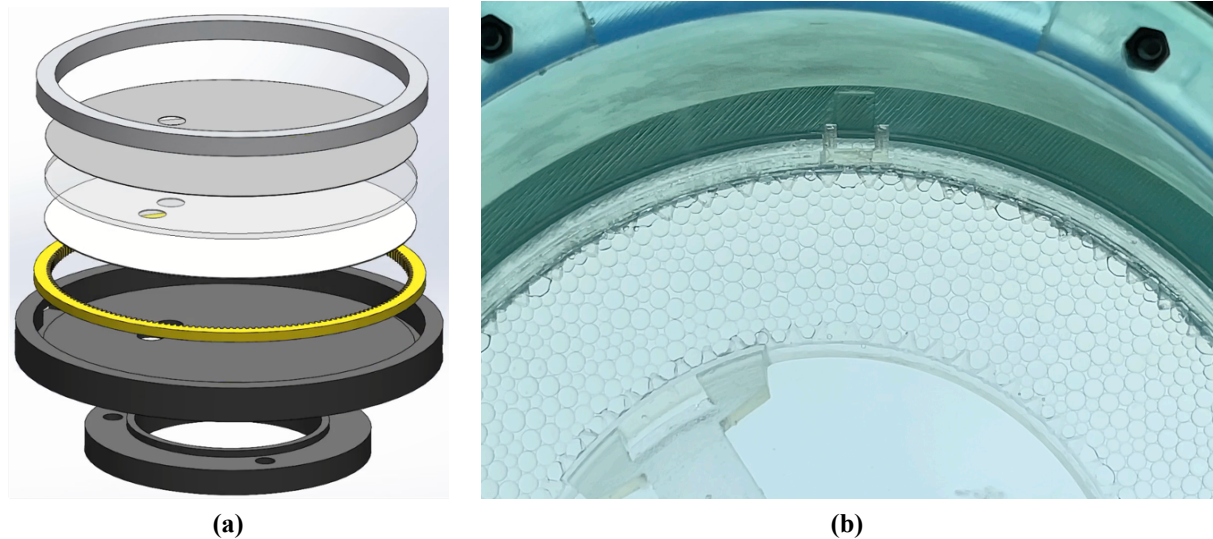


Figure 3.3: (a) A SolidWorks model of the background illumination system. From top to bottom are a centering ring, a diffusing paper, a glass diffuser, a reflecting paper, a LED stripe, a container and a connector to the rheometer. (b) An example of the experimental image.

3.2.3. Emulsion preparation

A bidisperse monolayer of emulsion is created in our experiments. The emulsion is required to be sufficiently stable to minimize the occurrence of coalescence, as the measurement takes a considerable amount of time. The sunflower oil droplets are blown through two different-sized needles and float on the surface of a sodium dodecyl sulfate (SDS) solution with a 5.4% (w/v) concentration. The image processing results, which will be discussed in detail in Chapter 4, confirm the bidispersity of monolayers, which statistically consist of droplets of 1.4 ± 0.1 and 1.9 ± 0.1 mm diameter, with an average diameter $\langle d \rangle = 1.6$ mm for all droplets, see Figure 3.4(a). Although the coarsening and coalescence cannot be entirely ruled out during the experiment, it remains confined within an acceptable range, as evidenced by the consistent distribution of droplet diameters over one revolution at rotational speed $\dot{\Omega} = 0.0086$ (rad/s).

Meanwhile, two needles connected to a syringe pump are inserted vertically into the solution (Figure 3.4(b)), which was found to improve the reproducibility of experiments, as droplets of similar diameter distribution were created for different experiments. Initially, horizontal needles were adopted for their ease of waterproofing, but we encountered a critical issue where oil droplets would crawl along the needle as they grew, remaining attached until achieving sufficient buoyancy. We observed that the crawling time and the droplet size were hard to control during experiments mainly due to a manufacturing precision issue: the diameter of the hole through which the needle passes slightly exceeds the needle diameter, causing an uncontrollable tilt in the ac-

tual experiment. Such deviations from the horizontal plane, approximately within the range of $-15^\circ \leq \theta \leq 15^\circ$, would result in undesirably significant variations in oil droplet size, rendering experimental control difficult. On the other hand, this manufacturing defect has less effect on vertically inserted needles within the uncertainty range of $-15^\circ \leq \theta - 90^\circ \leq 15^\circ$, as droplets left the needle directly. In addition, Vaseline was employed to seal the outside of the hole, and all tubes were meticulously fixed to prevent falling during the experiment.

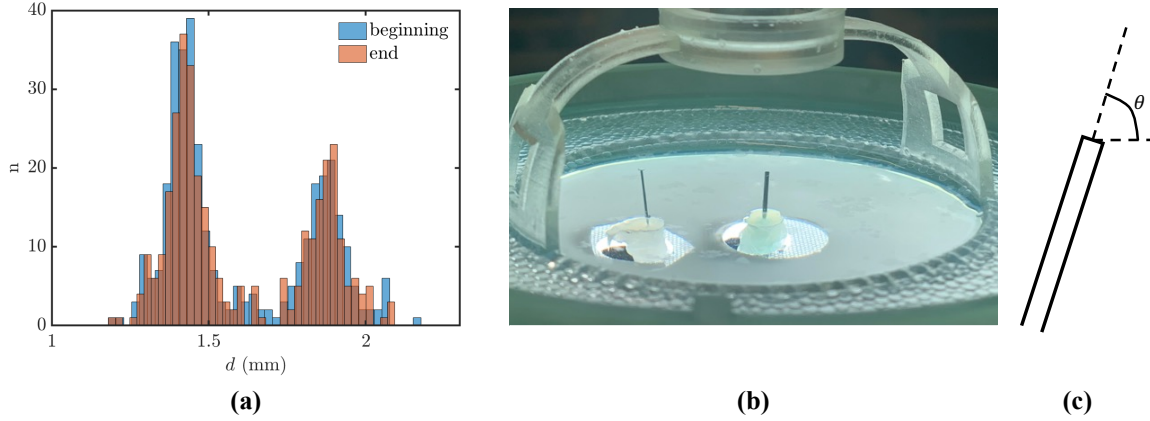


Figure 3.4: (a) The distribution of droplet diameters over one revolution at rotational speed $\dot{\Omega} = 0.0086$ (rad/s). The bidisperse monolayer consists of droplets of 1.4 ± 0.1 and 1.9 ± 0.1 mm diameter, with an average diameter $\langle d \rangle = 1.6$ mm for all droplets. (b) An experimental photo of two vertical needles with different diameters. (c) A sketch of the deviation angle from the horizontal plane.

3.3. Experimental methods

As previously discussed, our experiments aim to measure the steady flow curves of bidisperse emulsion monolayers, necessitating the coverage of a wide range of packing fraction ϕ and shear rates $\dot{\gamma}$. To establish an optimal experimental procedure, we conducted several trials to address the following questions concerning

- the duration of measurement. Due to the manufacturing defect, components like the inner ring and the cup are not perfectly symmetric in the azimuthal direction. Therefore the measurement duration should last at least one complete revolution for each rotational speed at a given droplet packing. By averaging the measured data over one period, we could mitigate the impact of azimuthal asymmetry and obtain representative results for the **steady** flow behavior. Our investigation delved into whether a single revolution measurement is sufficient to capture the steady flow properties and if the driving torque applied to the monolayer significantly breaks its structure, leading to changes in flow properties over time. A detailed discussion on this matter is presented in Section 3.3.1.
- the range of measurable torque. The torque involved in driving the emulsion monolayer is usually extraordinarily low, particularly at low rotational speeds ($T \approx 10^{-1} \mu\text{N} \cdot \text{m}$). Although the rheometer we adopted, Anton Paar MCR 302e, claims a minimum measurable torque of $1\text{nN} \cdot \text{m}$, special care was taken to measure such low torques accurately, see Section 3.3.2.
- the range of the packing fraction ϕ and the rotational speed $\dot{\Omega}$. While our setup allows for a wide range of ϕ and $\dot{\Omega}$, we specifically focused on exploring droplet packing around

and above the jamming point. In addition, we were curious to find whether we could reach the yield region in a macroscopic rheometrical measurement. The outcomes of these investigations will be presented in Section 3.3.3.

3.3.1. Measurement duration

To determine the necessary measurement duration, torque measurements were performed over twelve revolutions at different rotational speeds with a data acquisition frequency of 10 Hz, see Figure 3.5. Twelve repeating periods are observed at different rotational speeds, suggesting that the flow properties remain consistent throughout the long-duration measurements. Hence we

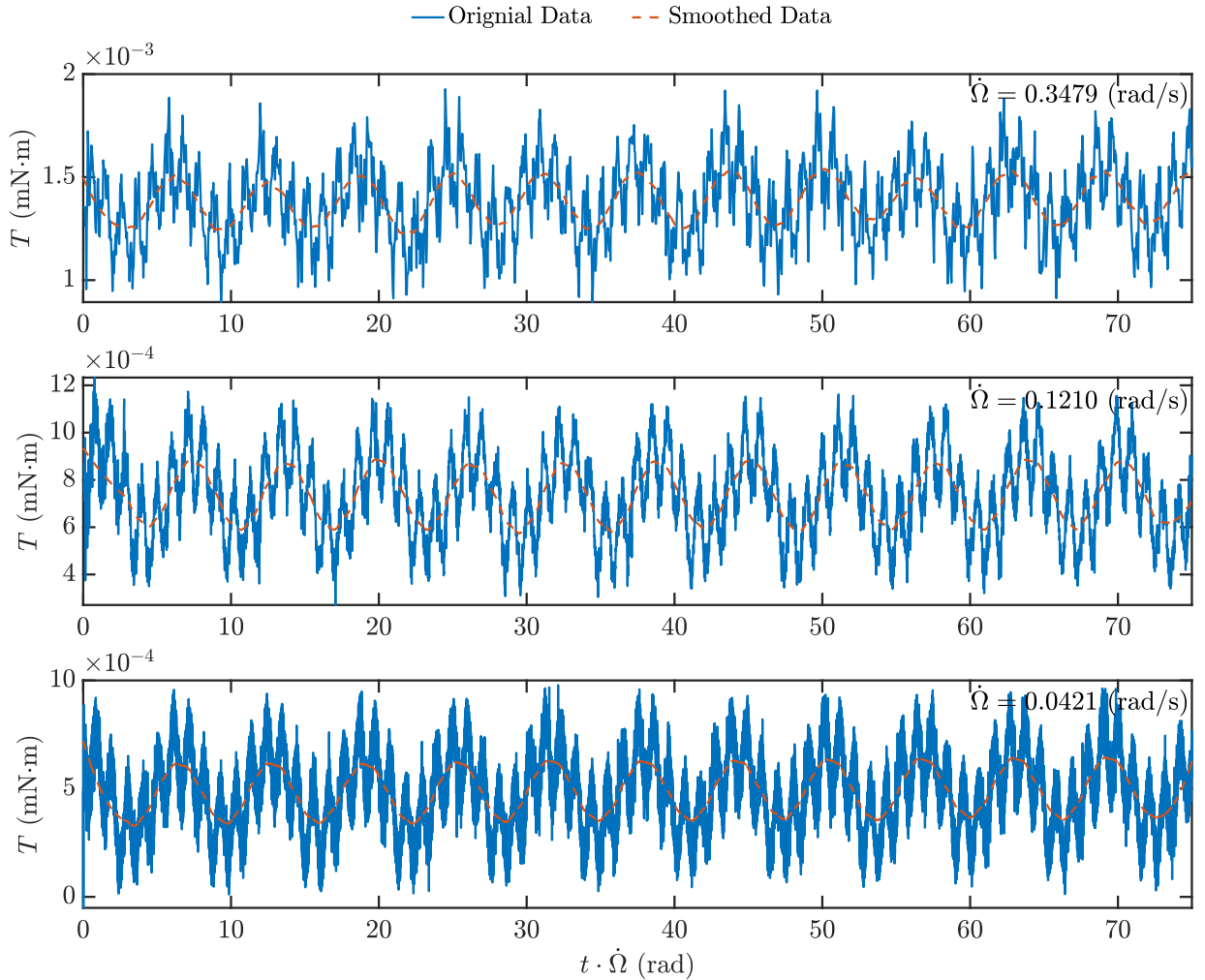


Figure 3.5: Torque measurements over twelve revolutions at different rotational speeds: $\dot{\Omega} = 0.3479, 0.1210, 0.0421$ (rad/s) respectively. The x-axis represents time normalized by the rotational speed, where 12 revolutions are equivalently represented by 24π . The y-axis is the measured torque, with varying ranges in the three plots: as the rotational speed decreases, the measured torque also decreases. The blue solid line represents the original data at a measurement frequency of 10 Hz, with the removal of outliers using a Hamper identifier. The red dashed line is the smoothed data obtained by filtering the measurements through a Savitzky-Golay finite impulse response (FIR) smoothing filter, which reveals 12 repeating periods.

infer that one complete revolution is sufficient to represent the steady rheological properties of the emulsion monolayer.

On the other hand, the consistency of results over 12 periods at different rotational speeds cor-

robustness of the stability of the emulsion monolayer, as the coalescence and coarsening induced by droplet motion have a marginal effect on the bulk torque measurement.

3.3.2. Low torque adjustment

In our experiments, a standard adjustment to the rheometer involves three essential steps:

1. Adjust the drive inertial without the measuring system.
2. Adjust the inertial of measuring system, i.e., the inner ring.
3. Adjust the upper motor with the measuring system.

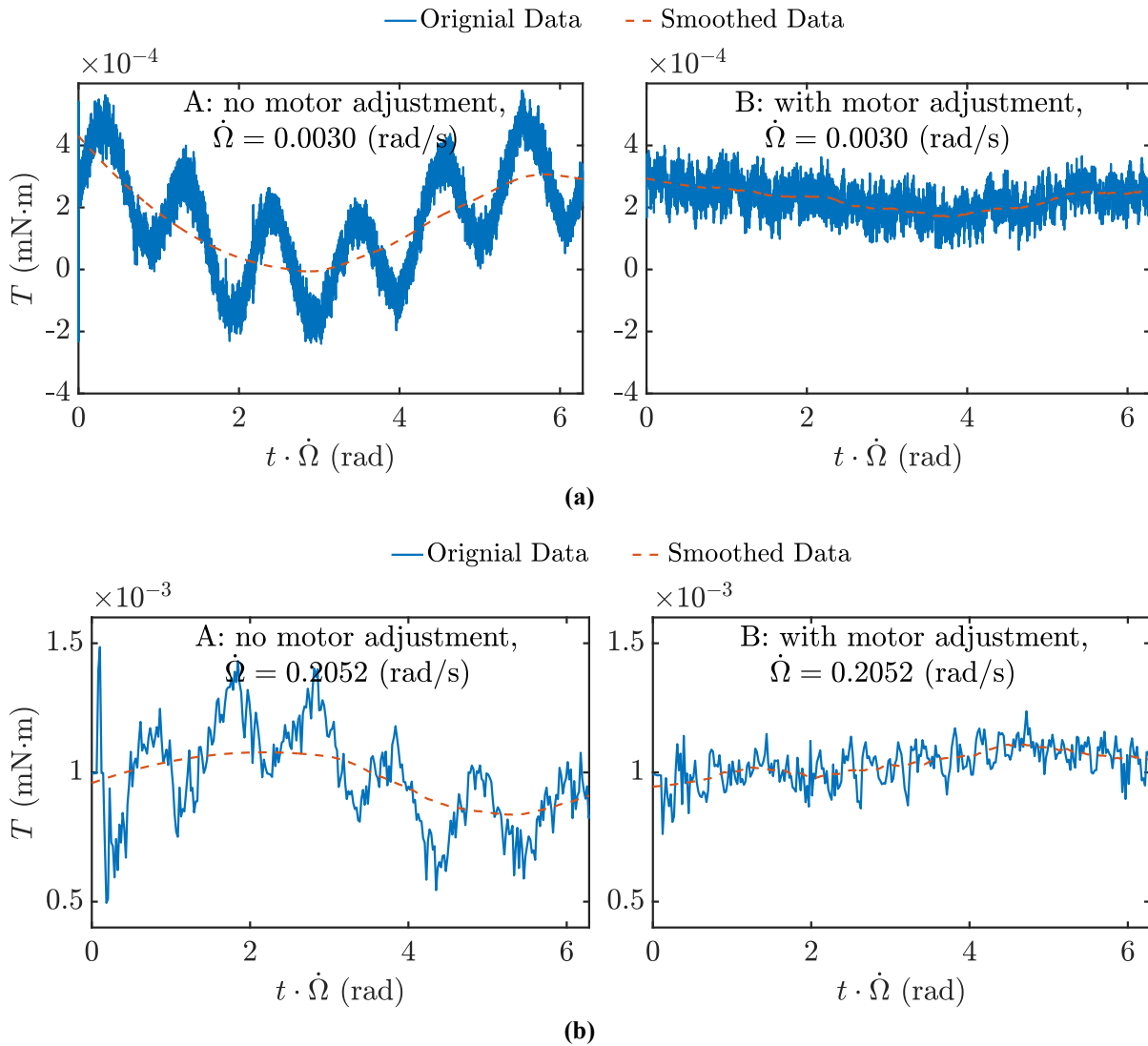


Figure 3.6: Comparison of torque measurements in two independent experiments: experiment A was performed without motor adjustment given $\phi = 0.9213 \pm 0.0039$ and experiment B was performed with motor adjustment given $\phi = 0.9188 \pm 0.0043$. (a) Torque measured over one revolution at a low rotational speed $\dot{\Omega} = 0.0030$ (rad/s). The left plot presents the results of experiment A, featuring a negative torque region and six smaller periods within one revolution. In contrast, the right plot displays the results of experiment B, demonstrating a more consistent trend within one revolution, attributed to the application of motor adjustment. The steady torque of two measurements vary significantly. (b) Torque measured over one revolution at a high rotational speed $\dot{\Omega} = 0.2052$ (rad/s). The steady torques of two experiments are comparable.

Typically, the first two steps are sufficient for a rheological measurement of common materials. However, in the case of interfacial rheological measurements, especially when dealing with extremely low torque, the extra third step is necessary to improve the reliability of the experimental data. To investigate the impact of motor adjustment on torque measurements, we conducted two independent experiments with similar packing fractions. Experiment A was performed without motor adjustment at a given packing fraction $\phi = 0.9213 \pm 0.0039$, while experiment B was performed with motor adjustment at $\phi = 0.9188 \pm 0.0043$. The evolution of the shear torque at both low and high rotational speeds is illustrated in Figure 3.6(a) and (b).

Experiment A, without motor adjustment, exhibits six smaller periods within one revolution at both low and high rotational speeds, raising doubts about whether they can be used for the analysis of steady flow properties. In contrast, experiment B presents a more consistent trend. A steady torque is defined as the medium value of the smoothed data. At high rotational speeds (Figure 3.6(b)), the steady torques of both experiments are comparable, although experiment A has a larger uncertainty (fluctuation range). However, at low rotational speeds (Figure 3.6(a)), the steady torque measurements vary significantly, and experiment A even displays a negative torque region, which highlights the necessity of motor adjustment to accurately measure low torques, reduce measurement uncertainty, and eliminate the occurrence of the smaller periods.

3.3.3. Range of $\dot{\Omega}$ and ϕ

To cover a range of $\dot{\Omega}$ and ϕ which is sufficient for analyzing the steady flow of emulsion monolayers, the final rheological measurement consisted of two alternating parts:

- continuously generating oil droplets and mixing the emulsion monolayer at a constant rotational speed 0.25 rad/s;
- Measuring the steady flow behavior at a set of logarithmically decreasing rotational speeds when the pump is stopped. The time interval between each stop is constant.

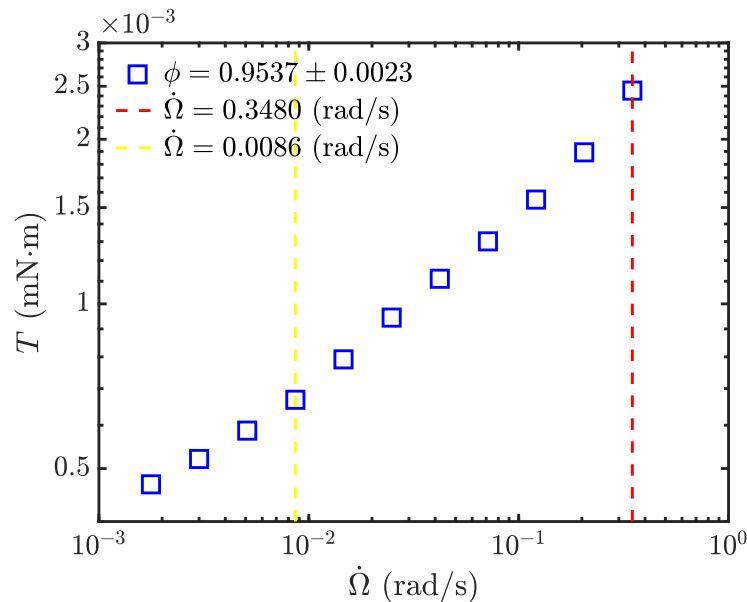


Figure 3.7: Steady torque vs. rotational speed (blue square) with packing fraction $\phi = 0.9537 \pm 0.0023$. The yellow line represent the lowest rotational velocity chosen for the final measurement, and the red line represents the highest.

However, two things remain to be determined: the range of rotational speeds and the lowest pack-

ing fraction for measurement, i.e., the first time for stopping the pump. Although in Section 3.3.1 we have shown that one revolution is sufficient for measuring the steady flow properties, the measurement lasts long, particularly at a low rotational speed. For instance, one revolution takes about 105 minutes at the $\dot{\Omega} = 0.001$ (rad/s). Therefore, the total duration is a concern since the measurements cover multiple packing fractions. Nevertheless, to investigate whether the macroscopic rheometrical measurement could reach the yield region of emulsion monolayers, a preliminary experiment covering rotational speeds of 0.001751 – 0.3480 (rad/s) was performed, see Figure 3.7. While the droplet packing is dense, around 0.95, the rotational speeds are not sufficiently low to measure the yield stress. Hence, the rotational speed region is reduced to 0.0086 – 0.3480 (rad/s), focusing on the shear thinning region, and later in the local rheological measurement (Chapter 5), yield behavior is observed. On the other hand, rotational speeds higher than 0.3480 (rad/s) are excluded because the fast-rotating oil droplets may detach from the inner ring, invalidating the no-slip boundary condition. Table 3.1 lists the final $\dot{\Omega}$ array.

An interesting phenomenon during the droplet-filling process is that the droplets prefer to first accumulate near the inner ring or the outer wall, i.e., they are “attracted” by the walls, known as the Cheerios effect [51]. The buoyancy of a floating droplet and the capillary force leads to the deformation of the liquid interface between droplets and between droplets and the wall, which manifests as attractive forces. Initially, the droplets clustering near the inner ring move together with the ring, while the droplets accumulating at the outer wall remain resting. Since two groups can not see each other, the solid-body rotation of the inner cluster mainly contributes to the torque measured by the rheometer. As droplets keep filling the surface, the gap between the two clusters decreases. When the inner cluster touches the outer cluster, the static packing is sheared to flow, implying a transfer of shear stress (drag) from the inner ring to the outer packing. Consequently, the measured torque increases dramatically once the outer packing is involved in shear flow. Figure 3.8 depicts the torque evolution over the droplet-filling process, mixing at a constant rotational speed 0.25 (rad/s). The evolution of torque experiences roughly two phases, with a slowly increasing phase followed by a steeply increasing phase.

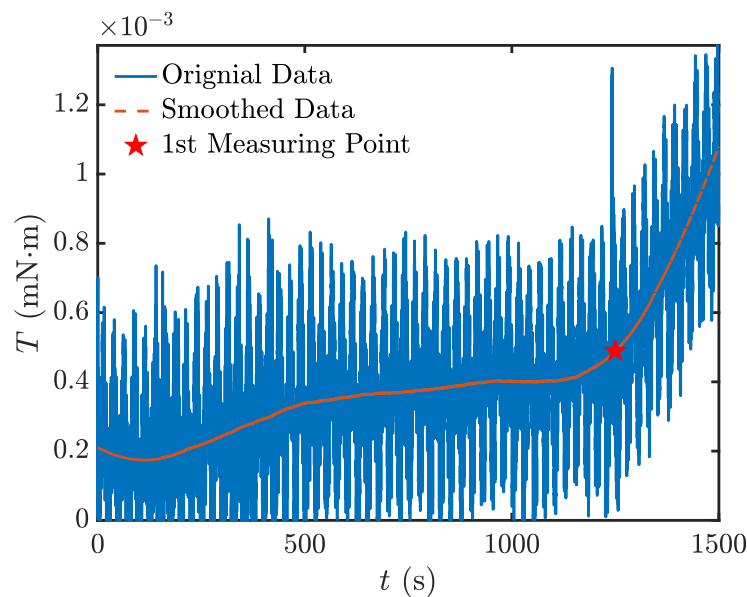


Figure 3.8: Torque evolution over the droplet-filling process, mixing at a constant rotational speed 0.25 (rad/s). The red pentagram represents the first time for stopping the pump.

The lowest packing fraction for measurement is the moment slightly after the transition from slow to steep increase, see the red pentagram in Figure 3.8. However, the exact moment for this transition and the distance of the first measurement point to the transition point cannot be quantified during the experiment because there is no communication between the pump and the rheometer. One practical choice is stopping the pump when the gap is close to vanishing at the mixing rotational 0.25 rad/s, as presented in Figure 3.9(a), so that the inner packing merely touches the outer packing at the lowest rotational velocity for the given number of droplets, see Figure 3.9(b). Section 5.1 will further illustrate such dependence of packing fraction on the rotational speeds: as the inner cluster rotates, the centrifugal force tends to push those droplets outside, competing with the attractive force from the wall.



(a)



(b)

Figure 3.9: The experimental image for the first measured droplet packing at (a) the highest rotational speed. (b) the lowest rotational speed.

3.3.4. Final experiments

In summary, the experiment consisted of two alternating parts:

- continuously generating oil droplets and mixing the emulsion monolayer at a constant rotational speed 0.25 rad/s; The flow rate is 0.1 ml/min for 30 ml syringe.

- Measuring the steady flow behavior at a set of logarithmically decreasing rotational speeds (Table 3.1) when the pump is stopped. The time interval between each stop is 60 seconds.

While measuring one revolution is sufficient for investigating the steady flow behavior, the process for each rotational speed lasted 1.2 revolutions in experiments to eliminate the inertia caused by the instantaneous changes between rotational speeds, and data taken after 0.2 cycles were used in the subsequent result processing.

Test No.	1	2	3	4	5	6	7	8
$\dot{\Omega}$ (rad/s)	0.3480	0.2052	0.1210	0.0714	0.0421	0.0248	0.0146	0.0086
v_0 (mm/s)	11.88	7.00	4.13	2.44	1.44	0.85	0.50	0.29

Table 3.1: Rotational speeds and corresponding rotational velocities measured for each volume fraction. Each measurement began with the highest speed.

Table 3.2 lists the measured volume fraction range, evaluated by the image analysis shown in the next chapter. The range quantity represents the ϕ_1 due to the azimuthal non-uniformity, and we will come back to it later in Section 5.1.

	ϕ_1	ϕ_2	ϕ_3	ϕ_4	ϕ_5	ϕ_6	ϕ_7	ϕ_8	ϕ_9
Input oil (ml)	0.00	0.10	0.20	0.30	0.40	0.50	0.60	0.70	0.80
ϕ	[0.4736, 0.8295]	0.8330 ± 0.0205	0.8552 ± 0.0082	0.8830 ± 0.0086	0.8992 ± 0.0065	0.9226 ± 0.0040	0.9344 ± 0.0027	0.9436 ± 0.0030	0.9468 ± 0.0021

Table 3.2: Volume fractions covered in the experiments.

Image analysis

The image analysis aims to obtain the velocity profile and packing fraction from the experimental imaging data. Particle image velocimetry (PIV) [40] and particle tracking velocimetry (PTV) [37] are two standard methods for acquiring a two-dimensional configuration's velocity profile. Our research adopted PTV due to its ability to identify droplets individually, offering the advantage of measuring droplet packing fractions simultaneously.

Experimental images were captured using an iPhone 12, with settings of 1080p resolution and 60 frames per second. Due to the refraction index difference between the oil and aqueous phases, the images exhibit three main components, the edges of oil droplets, the interiors of oil droplets, and the aqueous background, see Figure 4.1. While some droplet edges possess clarity (indicated by the black solid line), others appear indistinct (denoted by the red dashed line) due to the mutual deformation of oil droplets and the limitations of the image acquisition apparatus. Moreover, although the background region shares a similar light intensity with the interior of the droplets, their geometrical structures differ, rendering the image processing feasible.

The following sections present the particle tracking strategy in two parts: the processing of a single frame and the frame correlation. Within the single-frame processing, the first step entails segmenting the image into distinct regions and detecting mass centers of individual regions. The subsequent task involves computing the packing fraction, including droplet interiors and edges. In the second part, the frame correlation acquires the steady velocity profile.

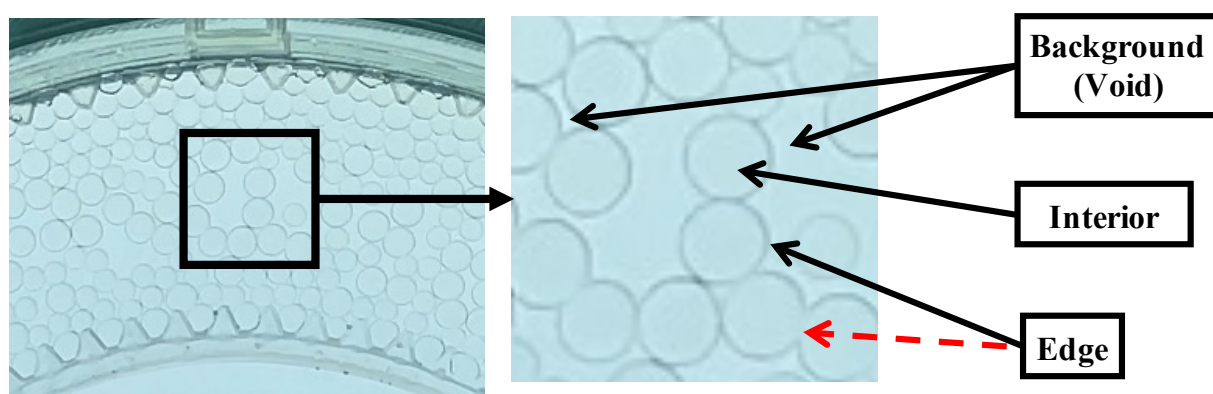


Figure 4.1: Three components of an experimental image: the aqueous background, the droplet interior, and the droplet edge.

Varied packing of droplets and rotational speeds lead to varying degrees of droplet deformation, along with different void sizes and shapes, which motivates the development of different pro-

cessing strategies depending on the concentration of droplets. Generally, the imaging data fall into three categories, high ϕ , medium ϕ , and low ϕ . In the high ϕ scenario, voids constitute approximately less than a tenth of the (averaged) droplet areas, indicating that the droplets have a distinct geometric difference from voids. However, when the droplets are less densely packed, voids emerge with similar areas and shapes as droplets, requiring additional steps to remove them; therefore, this scenario is classified as medium ϕ . In addition, gaps with various shapes exist at a significantly low packing fraction, while sometimes the edges between droplets with those large regions are indistinct, classified as low ϕ .

4.1. Image processing of single frame

Figure 4.2 depicts the approach for processing a single frame, encompassing three steps: image denoising and binarization, morphological operations, and masking of large voids. While the first two steps are sufficient for the high ϕ scenario, the third step facilitates the processing of medium and low ϕ .

4.1.1. Binarization and morphological operation

The binarization of images is straightforward but the most essential step, laying the foundation for subsequent processing. An intensity mapping is first employed, expanding the original intensity range to a broader spectrum and enhancing the contrast between the droplet edges and interiors. Following this, a Gaussian filter is applied to denoise the image, ensuring uniform intensity within the droplet interior, see Figure 4.2.B. The denoised grayscale image is then binarized with a locally adaptive threshold (dark foreground) algorithm to mitigate the slightly non-uniformity of background illumination. As depicted in Figure 4.2.C, most droplet edges have been effectively eliminated, leaving behind only the distinct interior regions and voids.

Some tiny binarized voids can be removed by an area filter, as shown in Figure 4.2.D. Several problematic regions are highlighted with different colors. The blue square presents the connected region after binarization, introducing challenges in center detection. The yellow and pink squares highlight the bottleneck-shaped configuration, formed by one droplet and a void or by two droplets. The red squares denote voids with similar area or eccentricity as droplets, commonly encountered in medium and low ϕ scenarios, and we will discuss it in Section 4.1.2. The droplet-connected regions and some of the bottleneck shapes can be addressed by applying the watershed transformation, which effectively segments contiguous regions into distinct objects (Figure 4.2.E.2). While the watershed method typically operates on the distance transformation of the binary image, it tends to over-segment the droplets in this case. The issue is mitigated by introducing minima to the distance transformation process. The image is subsequently subjected to an erosion process, followed by a dilation morphological operation utilizing a disk-shaped structural element, as depicted in Figure 4.2.E.3. In this stage, the remaining bottleneck is degenerate to a droplet region (the pink square), while simultaneously, the segmented regions are smoothed to be more circular morphology (the yellow square). These binarization and morphological operations are adequate for the high ϕ scenario.

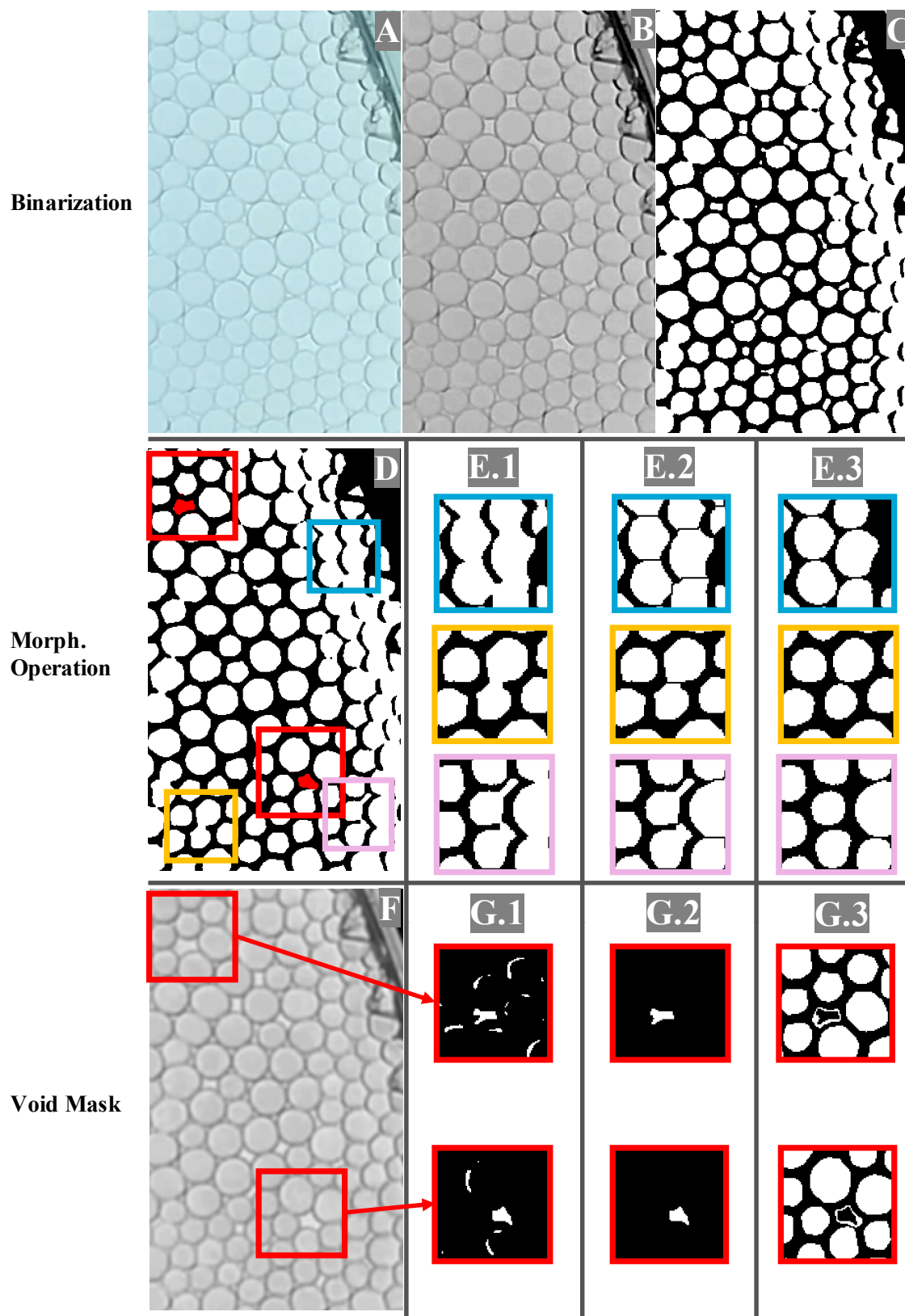


Figure 4.2: Single-frame processing. A-C: original, filtered and binary image; D: small-area filtered image; E.1-3: watershed and morphological operation; F: histogram equalization; G.1-3: steps of masking large voids.

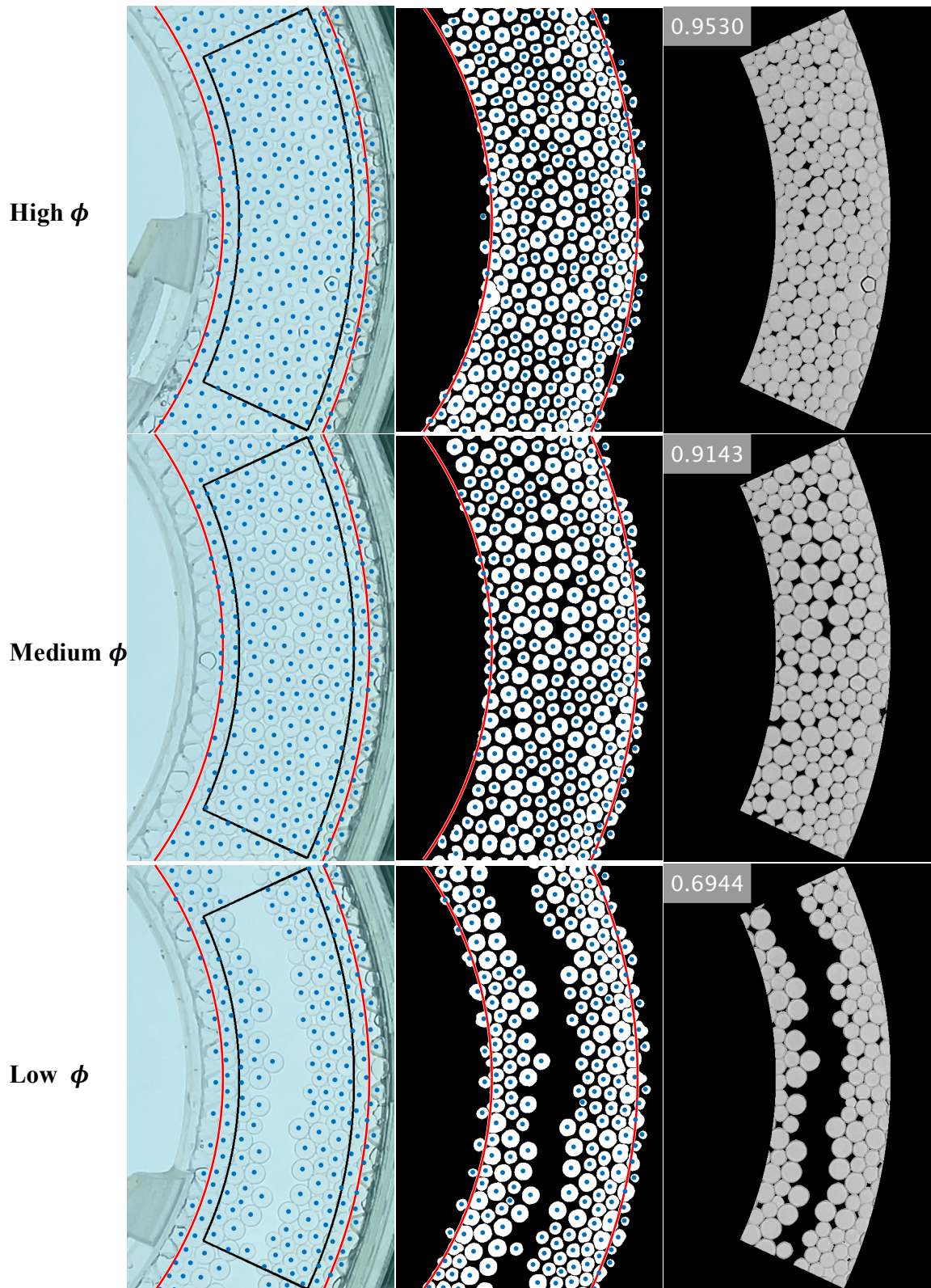


Figure 4.3: Validation of droplet identification and packing fraction. The first column presents original images with the droplet centers detected. The corresponding binary images are shown in the second column. The third column depicts the area fraction occupied by droplets within the black fan-shaped region.

4.1.2. Large void mask

With morphological operations and various region filtering criteria such as area and eccentricity, small voids are removed. However, some voids possessing geometry features resembling droplets may confuse the center detector. As depicted in Figure 4.2.D, red squares highlight these problematic voids, which exhibit similar areas to small-size droplets or comparable eccentricity to the deformed droplets near the wall, invalidating the region filters.

The voids usually exhibit a slightly brighter appearance than the interior of the droplets, see Figure 4.2.B. Image sharpening and adaptive histogram equalization can be adopted to enhance the contrast further, resulting in Figure 4.2.F. Binarized with a locally adaptive threshold (bright foreground), the majority of the large voids, together with some noising regions from the droplets, are masked out, as shown in Figure 4.2.G.1. The noising regions are then filtered with the morphologically opening operation, preserving the center of large voids (Figure 4.2.G.2). By applying logical *NOT* operation between Figure 4.2.G.2 and E.3, the interior of large voids can be masked out (Figure 4.2.G.3), while the region filtered or morphological operations are followed to remove the residuals. The large void masks, combined with the previous binarization and morphological operations, are well-suited for the medium ϕ scenario.

Furthermore, in the low ϕ case, there exist super large background regions several times the droplet sizes, which remain connected with droplet regions after the binarization, see the left image in Figure 4.4 (the connected part is highlighted with red). A watershed transformation can not be directly applied to segment those droplets from the background. Otherwise, the large background will be segmented into several smaller parts, as depicted in the middle image of Figure 4.4. Some of those small parts have similar geometry features to droplets (the blue region), which may be detected as fake ones.

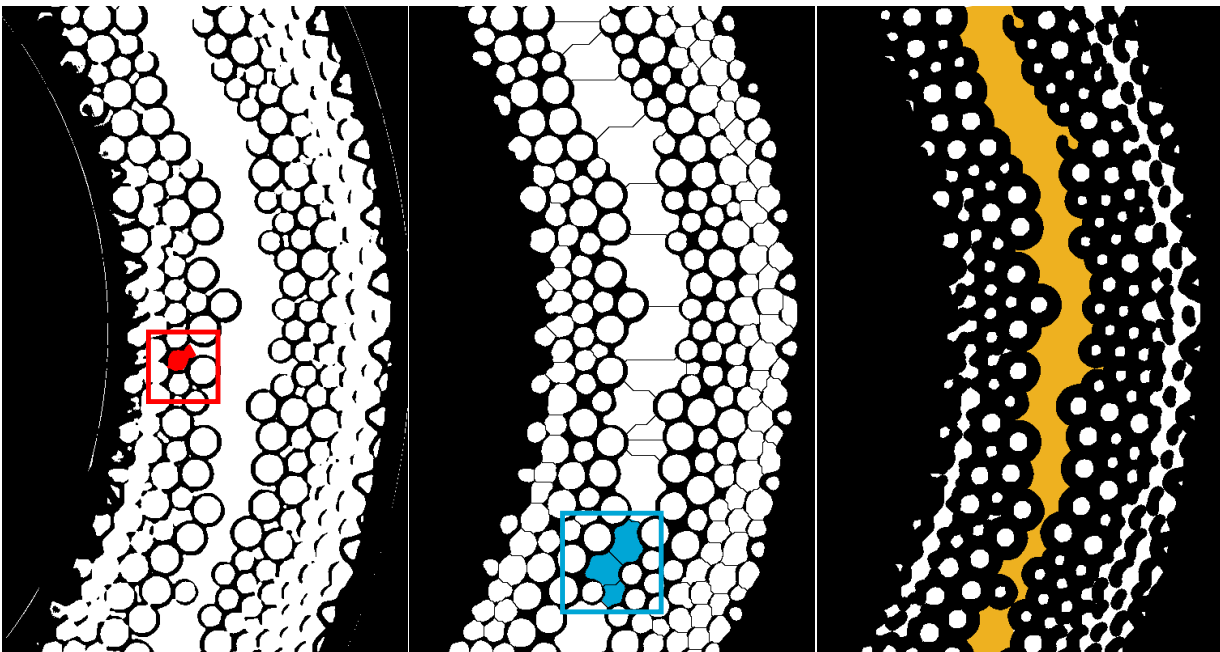


Figure 4.4: Steps for removing large gaps in the low ϕ scenario.

One possible solution is to erode the image and filter large areas (the orange region). However, the connected areas near the walls are interfering. Hence, A ring-shaped position mask is adopted

to distinguish the gaps in the middle from the distractors near the walls, given that droplets tend to gather near the wall and the large gaps only appear in the middle of the surface. Finally, a dilation operation restores the eroded regions to their original size.

4.1.3. Validation: droplet identification

With all noises from the voids and droplet edges removed, the remaining disconnected regions in the binary image are individual droplets, which we could further apply analysis of region properties to acquire information such as the mass center and area. The mass centers of all regions are scattered on the original image to preliminarily validate whether the single frame processing works well, as presented in Figure 4.3 for high, medium, and low ϕ respectively. The first and second columns present the experimental and binary images, where the red lines represent the inner and outer radii, and the blue solid dots are the centers detected.

Some remarks for the droplet identification are summarized as follows:

- For high and medium ϕ cases, the method can detect all droplets and filter all the voids within the black fan-shaped region, which is of the most interest. For low ϕ packing, although there exist a few undetected droplets and falsely detected voids in this region, we can merely content ourselves that these errors are insignificant compared to the errors brought by large gaps.
- For all three cases, the method can only detect part of droplets near the walls, and some teeth-shape regions are misrecognized as droplets. Furthermore, some droplet regions near the walls remain connected. However, as will be shown in Section 4.2, the acquired information is sufficient for measuring the velocity profile.

4.1.4. Validation: packing fraction

The binary image of droplet interior regions can be further dilated with a disk structural element of a 4-pixel radius to include the droplet edge regions, from which the packing fraction occupied by droplets is measured. The validation of packing fraction measurement is presented in the third column of Figure 4.3, together with the packing fraction within the black fan-shaped region.

At first glance, the results are satisfying, with most droplet interior and edge regions included and apparent voids masked out for all three cases. Therefore, the calculated packing fraction can feature the extent of the droplet packing. For the low ϕ case, the big gap is successfully masked out, with only a small part remaining, which is sufficient for a preliminary analysis. Of course, the value calculated in one single frame is insufficient to describe the global droplet packing, and a data analysis of ϕ s in different frames is followed in Section 5.1 to determine the most representative value of ϕ .

Zooming in, one may notice that the dilating operation recovers the droplet contours well in the middle region while overdone near the walls. In addition, the calculated packing fraction is sensitive to the threshold used for the image binarization. In the high ϕ scenario, for example, while the chosen threshold 0.601 gives $\phi = 0.9530$, a slightly small threshold 0.600 changes the packing fraction to $\phi = 0.9554$ and an increased threshold 0.602 resulting in $\phi = 0.9507$. It is hard to tell the difference between the three with the naked eye. Those seemingly negligible errors, however, really matter for the research on complex fluids.

4.2. Velocity profile: frame correlation

In order to track droplets over multiple frames, a frame correlation step is performed to link droplets with the nearest neighbor search based on a k -dimensional tree algorithm. Since the segmentation method sometimes fails near the wall region, some droplets may be successfully detected in the current frame but are misrecognized as one droplet in the next frame. Therefore an extra criterion that the area difference between the two linked droplets must be less than ten percent is adopted, resulting in some detected centers unmatched between adjacent frames. Figure 4.5 shows the frame correlation results, where the blue and red color represent the detected center in the current and next frames, respectively; the solid and open circles represent the matched and unmatched centers, respectively. A zoom-in view of different regions is shown in Figure 4.5 as well, demonstrating that the area-matching criterion works well for filtering the falsely detected centers.

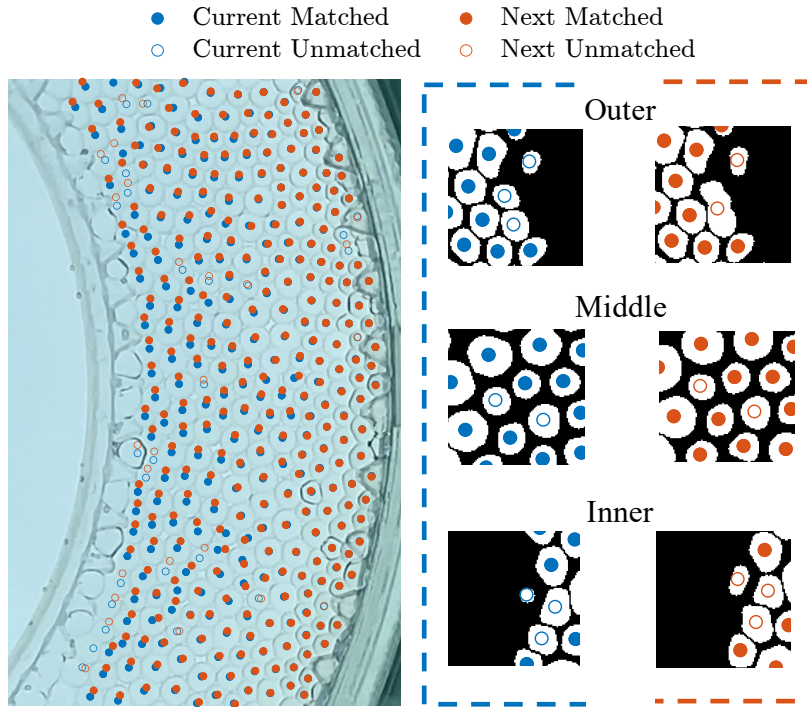


Figure 4.5: Validation of frame correlation. On the right are the zoom-in views of the inner, the middle, and the outer regions.

Once the centers in the current frame are matched with those in the next frame, an instantaneous velocity field can be calculated as the radial and azimuthal components in a polar coordinate. By averaging the instant velocity field over all the frames, *steady* radial and azimuthal velocity profiles can be determined. A one-dimensional staggered grid is adopted for a discrete description of the velocity profile and the corresponding local shear rate, see Figure 4.6. While the velocity profile is evaluated at the midpoints, the local shear rates and shear stress are determined at the integer points. Although the inner radius R_i and the outer radius R_o are initially defined as the outer edge of the tooth-shaped wall, later we will see that a preferred choice of the inner radius is $R_i^{\text{new}} = R_i^{\text{old}} - 0.5 \langle d \rangle$ for better matching the no-slip boundary condition. In addition, with two extra points $r_{1/2}$ and $r_{N+3/2}$, the motion of droplets within the first and the last rows are captured.

A practical choice of bin number is $N = \lceil (R_o - R_i) / \langle d \rangle \rceil = 9$. The resulting velocity

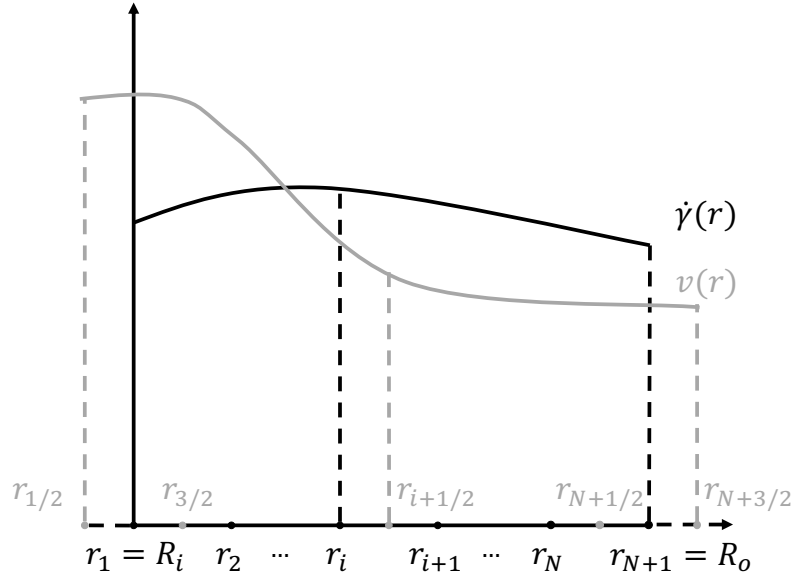


Figure 4.6: The sketch of a one-dimensional staggered grid for a discrete description of steady azimuthal velocity and local shear rates.

profiles are compared with $N = 90$ in Figure 4.7(a), where the two cases exhibit consistent trends. The normalized azimuthal velocity is approximately equal to one, implying a valid no-slip boundary condition. The normalized radial velocity slightly fluctuates around zero, indicating the steady flow is radius independent.

As experimental images were taken at 60 fps, the number of images varied significantly for different rotational velocities. For example, one revolution at $\dot{\Omega} = 0.3480$ rad/s creates 1083 images, and creates 43836 images at $\dot{\Omega} = 0.0086$ rad/s. Therefore for a given rotational speed, every M th frame is chosen for the correlation step, and a frame rotational speed is defined as

$$\dot{\Omega}_{\text{frame}} = \frac{\dot{\Omega}}{\text{fps}} \cdot M(\dot{\Omega}) \quad [\text{rad/frame}], \quad (4.1)$$

where $\text{fps} = 60$ and the integer M is $\dot{\Omega}$ -dependent. $\dot{\Omega}_{\text{frame}}$ should be the same for image series of different rotational speeds so that the resolution of the processing method is consistent. Figure 4.7(b) presents a comparison between different $\dot{\Omega}_{\text{frame}}$. While the two results show similar trends and comparable error bars, a larger $\dot{\Omega}_{\text{frame}}$ is preferred to reduce the computing cost. A smaller error bar does not imply that a larger $\dot{\Omega}_{\text{frame}}$ is more accurate, but instead that it captures a smaller intensity of instantaneous velocity.

In the end, $N = 9$ and $\dot{\Omega}_{\text{frame}} = 0.016$ (rad/s) are chosen for the following image analysis. Accordingly, the velocity profiles plotted in Figure 4.7 with this setting were obtained by averaging [1174, 11126, 18845, 20228, 21903, 24392, 26439, 29414, 35929, 38627, 11031] valid and correlated centers at the 11 midpoints, respectively. The velocity data at each midpoint exhibit Gaussian distributions.

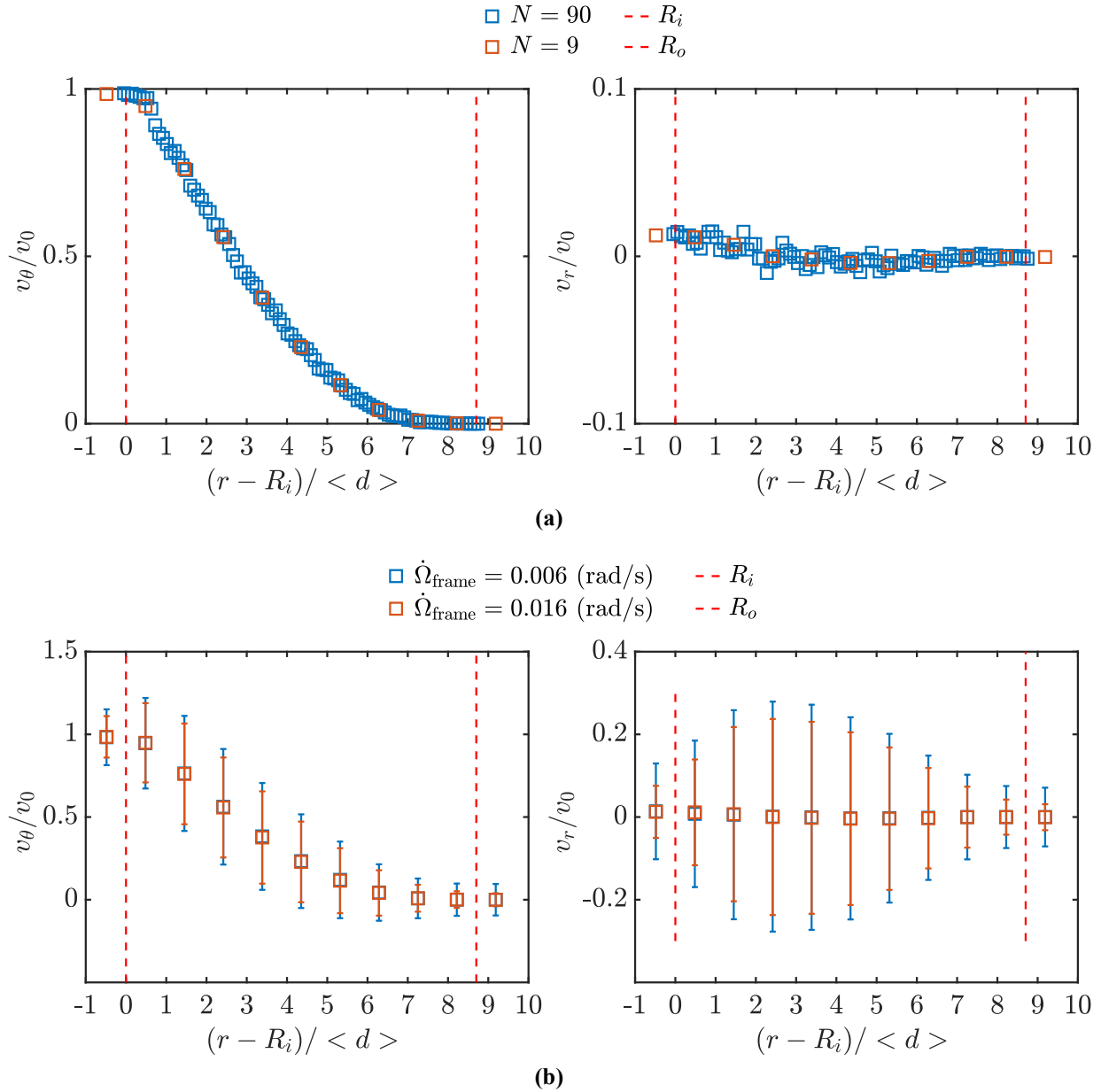


Figure 4.7: The velocity normalized by the rotational velocity v_0 versus the normalized radius. (a) A comparison between different bin numbers. (b) A comparison between different frame rotational speeds.

Results and discussions

As summarized in Table 3.1 and Table 3.2, the main results were obtained from an experiment with nine pump stops. In Section 5.1, we present the packing fraction profile obtained for all the measurements. The velocity profiles are displayed in Section 5.2. The macroscopic and local flow curves are analyzed in Section 5.3.

5.1. Packing fraction ϕ

In the two-dimensional configuration, the packing fraction is practically defined as the area fraction, i.e., the ratio between the total cross-section area of the emulsion oil droplets observed from above and the whole liquid surface area. As depicted before in Section 3.3.3, capillary force creates the deformation of the liquid surface at the inner and outer walls, leading to a tendency for droplets to accumulate nearby. This radial non-uniformity of packing fraction is observed in image analysis results that the packing fraction is higher at the inner and outer radii and reaches a minimum near the middle region, both in dilute and dense droplet packings, see Figure 5.1.

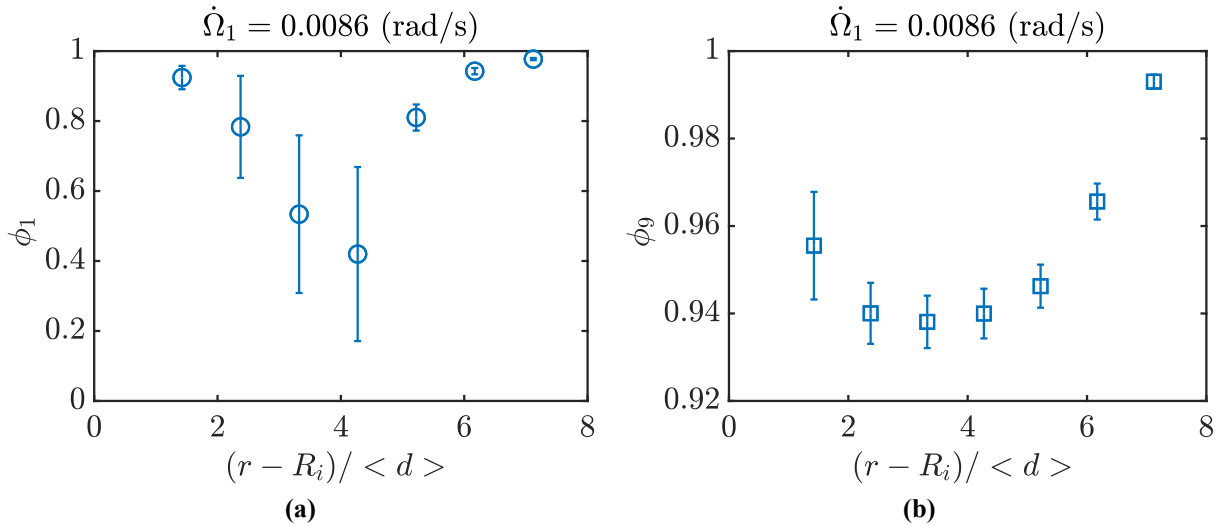


Figure 5.1: Average packing fraction profile in one revolution.

In addition, an azimuthal non-uniformity emerges in dilute packing, see Figure 5.2(c), where the evolution of packing fraction within one revolution is depicted. Here, two different regions of interest (ROIs) are chosen for the ϕ measurement, as depicted in Figure 5.2(a) and (b), and

the ROI encloses more areas near the walls (represented by blue color) gives a higher packing fraction. For the denser packing, the azimuthal distribution is more consistent, implying that the time (azimuthal) averaged packing fraction is sufficient to represent a *steady* flow of emulsion, as displayed in Figure 5.2(d).

Despite ϕ^l is always larger than ϕ^s , they exhibit similar trends, suggesting that adopting different ROIs only affects the magnitude of the packing fractions, other than their distribution properties. Therefore either ϕ^l or ϕ^s serves to characterize the denseness of droplet packing.

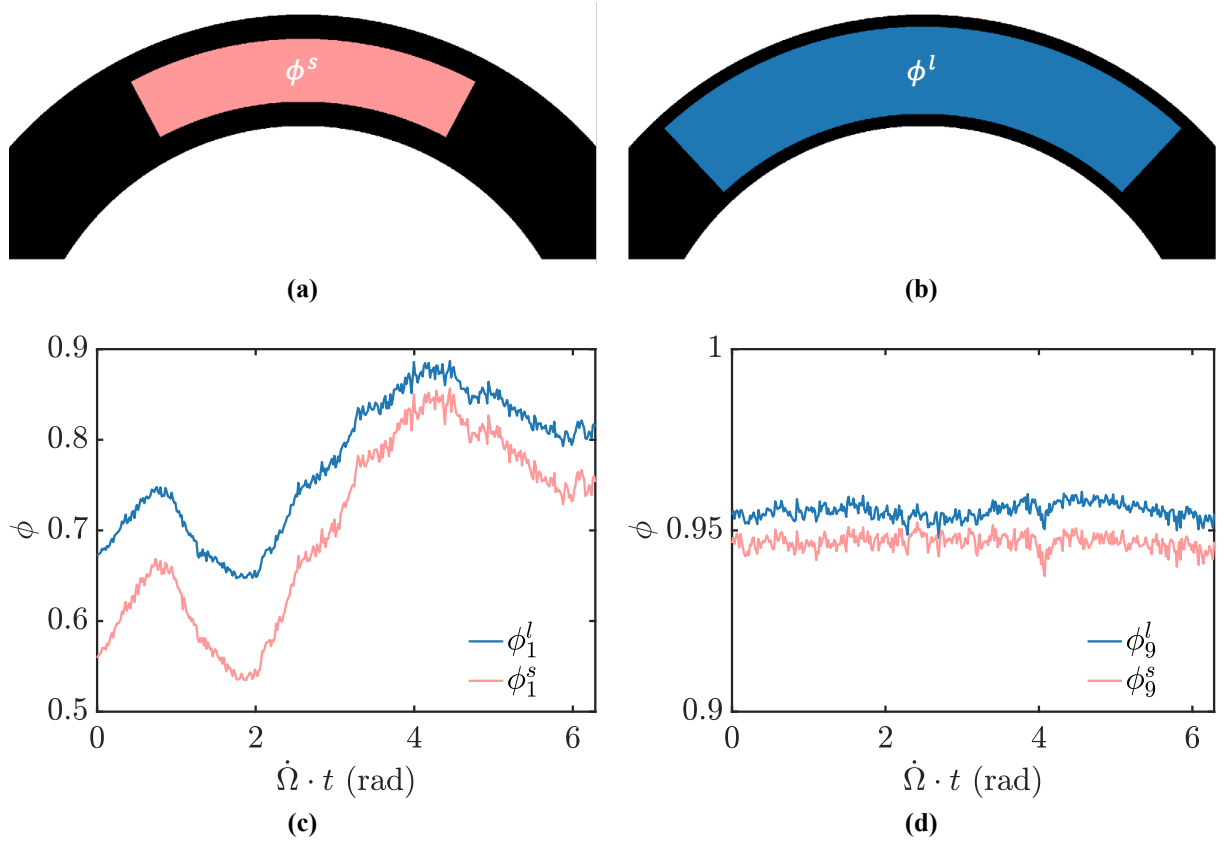


Figure 5.2: (a) Sketch of the small ROI (pink part) with the range $\{38.0 \leq r \leq 45.8 \text{ (mm)}, -28 \leq \theta \leq 28 \text{ (}^\circ\text{)}\}$; the result is labeled as ϕ^s . (b) Sketch of the large ROI (blue part) with the range $\{36.5 \leq r \leq 47.3 \text{ (mm)}, -43 \leq \theta \leq 43 \text{ (}^\circ\text{)}\}$; ϕ^l denotes the emulsion packing fraction in this region. (c-d) Distribution of the packing fractions in azimuthal direction. The subscripts are consistent with those in the Table 3.2.

As discussed in Section 3.3.3, another observation in the experiment is that droplets are attractive to each other, which may be explained by the existence of depletion force, and that with floating droplets deforming the interface, the buoyancy pulls them together or to the walls. For the shear flow in a cylindrical Couette cup, there exists a competition between the imposed centrifugal force and the attractive interaction, leading to different extents of deformation of the oil droplets at various rotational speeds. Hence, the measured packing fraction is $\dot{\Omega}$ -dependent, as shown in Figure 5.3. Since the packing fraction is usually calculated with a static subject [35, 52, 53], ϕ^s at the lowest rotational speed is chosen to represent the density of emulsion, where the droplets are the most relaxing. The corresponding values are summarized in Table 3.2.

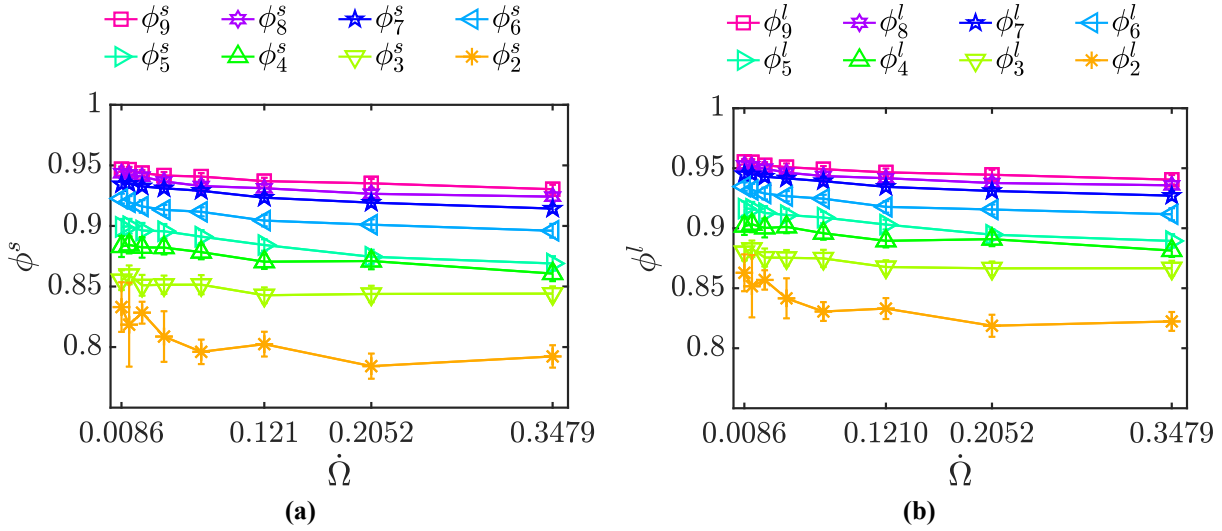


Figure 5.3: Packing fractions at different rotational speeds. Different symbols represent different droplet packings.

5.2. Velocity profile

The velocity profiles at various rotational velocities when $\phi = 0.9468$ are presented in Figure 5.4(a). Velocity profiles at $v_0 = 0.29$ (mm/s) for different volume fractions are displayed in Figure 5.4(b). For reference of remaining results, see Figure 5.7 and Figure 5.8.

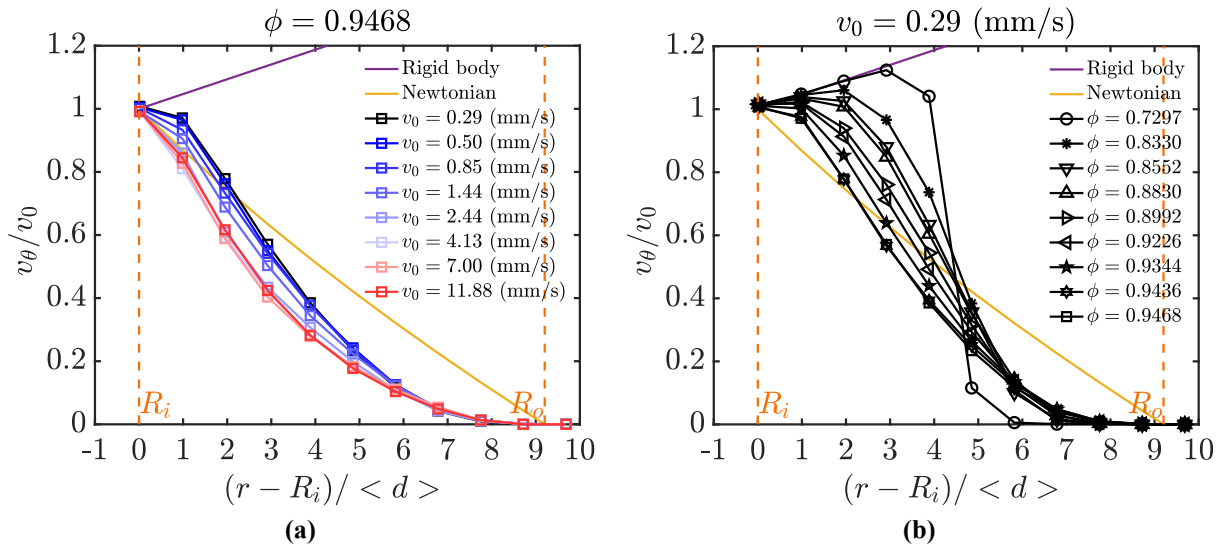


Figure 5.4: (a) The steady azimuthal velocity profiles at different rotational speeds (represented by different colors) for $\phi = 0.9468$. The vertical coordinate is the velocity normalized by the inner wall speed, i.e., $v_0 = \dot{\Omega}R_i$; the horizontal coordinate is the normalized radius with respect to the average diameter of droplets. Plots of other droplet packings are shown in Figure 5.7. (b) The steady azimuthal velocity profiles for various droplet packings (represented by various symbols) at the same rotational speed. For plots of other rotational speeds, see Figure 5.8.

The first observation is that velocity profiles exhibit a shear localization region near the outer wall within the experimental accuracy. Given the distribution of shear stress in the cylindrical Couette geometry, the localized profile indicates the existence of yield stress. For higher packing fractions,

the localized regions are rate-independent, see Figure 5.7(d-h). In addition, the curvature of velocity profiles indicates the shear rate decreases more rapidly as shear stress decreases (i.e., the radial coordinate increases) than for a Newtonian fluid within a certain range of radius, implying that the emulsion monolayer is shear thinning ([53]).

The velocity profiles exhibit different shapes near the inner wall, and we will see later that in this region, the shear rates even increase as shear stress decreases, which is unusual and indicates that the inner wall exerting an extra attractive force on the droplets has a significant effect on the flow behavior. Although we need more time for a detailed investigation of this wall effect, two preliminary observations can be made based on the current results. First, the extra attractive force makes the droplets closer to the inner wall move faster than expected for a shear-thinning flow and even exhibit rigid body rotation within a certain range when the packing fraction or the rotational speed is low. Second, the wall effect dissipates quickly in radius, i.e., it only significantly affects one or two rows of droplets outside the inner wall. Also, the wall effect becomes weaker when the packing fraction increases or at higher rotational velocities. In addition, the wall effect contributes to the non-uniformity of the packing fraction profile, which may also influence the flow behavior [54].

5.3. Macroscopic and local flow curves

Figure 5.5 plots the interfacial shear stress versus shear rates at the inner wall. Since the constitutive relation is unknown at this stage and accurate shear rates at the wall are impossible to be calculated, the shear rates plotted here are calculated by supposing a Newtonian fluid. Al-

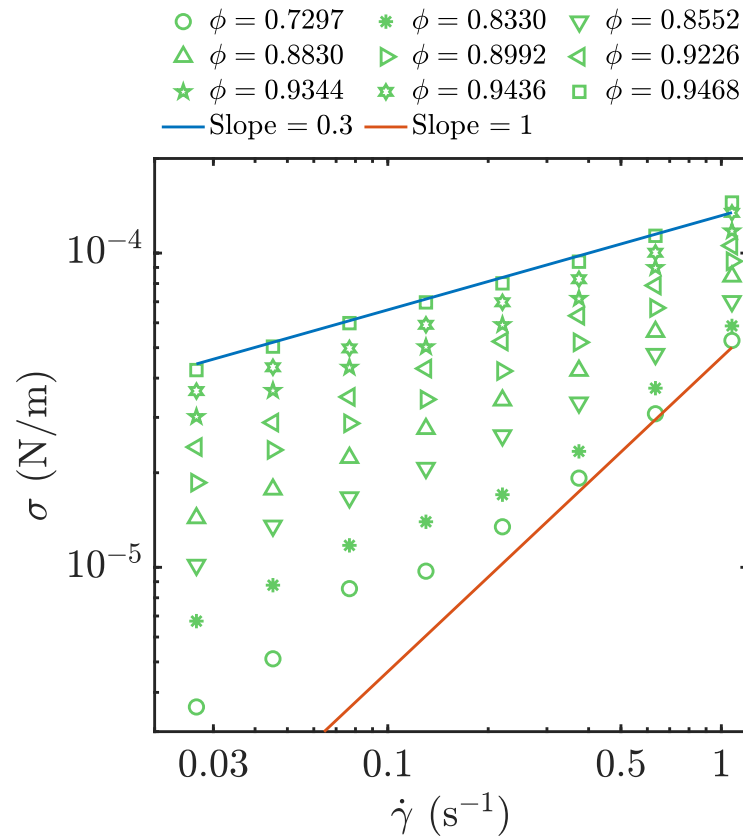


Figure 5.5: The flow curves at the inner wall. The shear rates are calculated with a Newtonian flow assumption.

though this is a rough assumption, an apparent **shear thinning** behavior (blue solid line) can be observed for dense droplet packings. In addition, as the packing fraction decreases, the flow exhibits Newtonian-like behavior at high rotational speeds.

On the other hand, thanks to the cylindrical Couette configuration and the no-slip wall condition, the local shear stress is expressed as $\sigma = \frac{T}{2\pi r^2}$ and the local shear rate can be derived from the velocity profile as $\dot{\gamma} = \frac{v_\theta}{r} - \frac{\partial v_\theta}{\partial r}$. Figure 5.6(a) presents the local shear rates when $\phi = 0.9468$. Close to the inner wall, the shear rates increase as the radius increases (i.e., the shear stress decrease) within two droplet diameters for high rotational speeds and three droplet diameters for low rotational speeds. Outside this region, the shear rates decrease much faster as the radius increases than for a Newtonian fluid, as expected for a shear-thinning fluid.

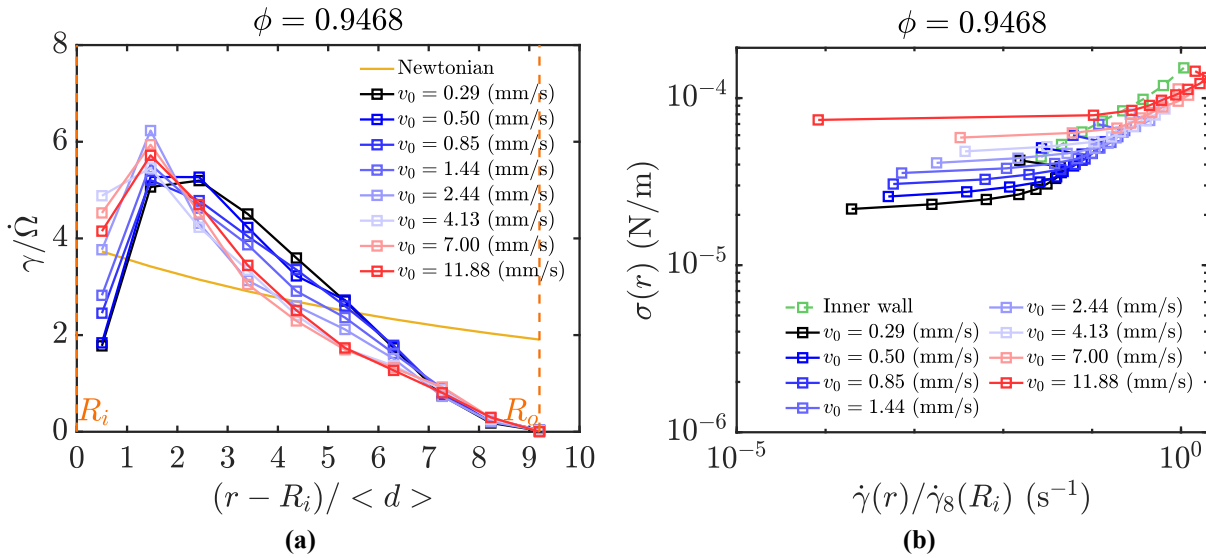


Figure 5.6: (a) The local flow rates. (b) The local flow curves. The green dashed line represents the relation between the shear stress (derived from the Torque measurement) and the shear rate (assuming a Newtonian flow) at the inner wall. The local flow curves for other droplet packings are summarized in Figure 5.10.

Since we know the shear stress and shear rate at every point within the gap, it is possible to plot the local flow curves with $\sigma(r)$ versus $\dot{\gamma}(r)$, see Figure 5.6(b), where three observations are summarized. First, the absence of a collapse of the local flow curves at different rotational speeds indicates that the **non-local effect** exists [40, 55]. Otherwise, the local flow curves should collapse into a master curve, as reported by [9, 53, 55]. The radial non-uniformity of the packing fraction may also contribute to the collapse's absence since the suspension viscosity depends on the packing fraction significantly [54, 56]. Second, each local flow curve possesses a boomerang shape, with the short-head part corresponding to the positive slope in Figure 5.6(a), indicating the **wall effect**. Third, each flow curve exhibits a plateau at low local shear rates, which further implies that the emulsion monolayer is a **yield stress material**.

In conclusion, the velocity profiles and the local flow curves show that the emulsion monolayer is a shear thinning yield stress material, even though we have not confirmed it in the macroscopic measurement (Section 3.3.2). However, the gap for filling the droplets is not wide enough to mitigate the non-local effect, which makes the universal scaling analysis impossible at the current stage. In addition, the wall effect and non-uniformity of packing fraction make the analysis more complex, calling for deeper investigation, and a brief discussion is presented in the next section.

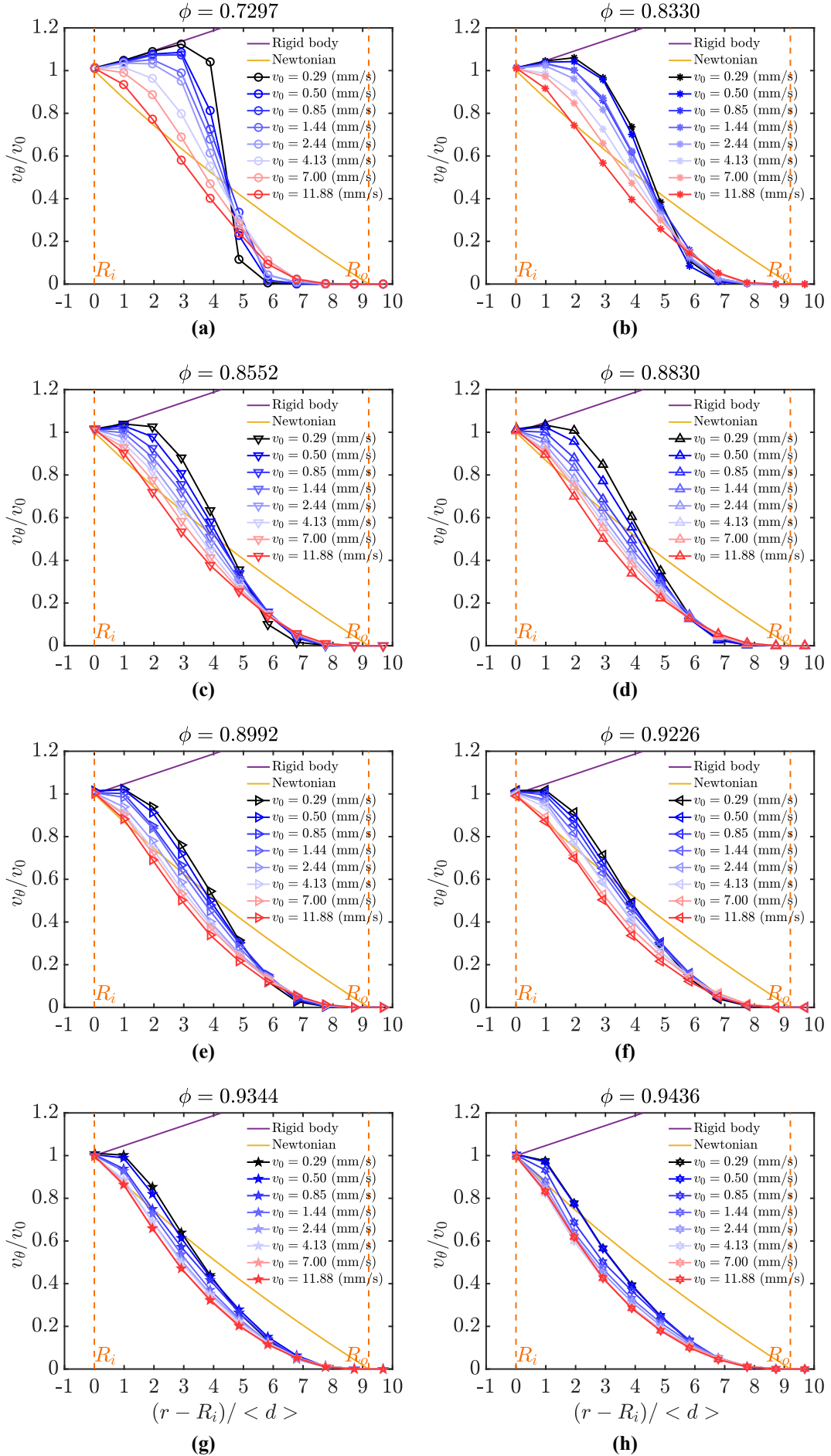


Figure 5.7: Velocity profiles at different rotational speeds (represented by different colors) for a given droplet packing (expressed by various symbols).

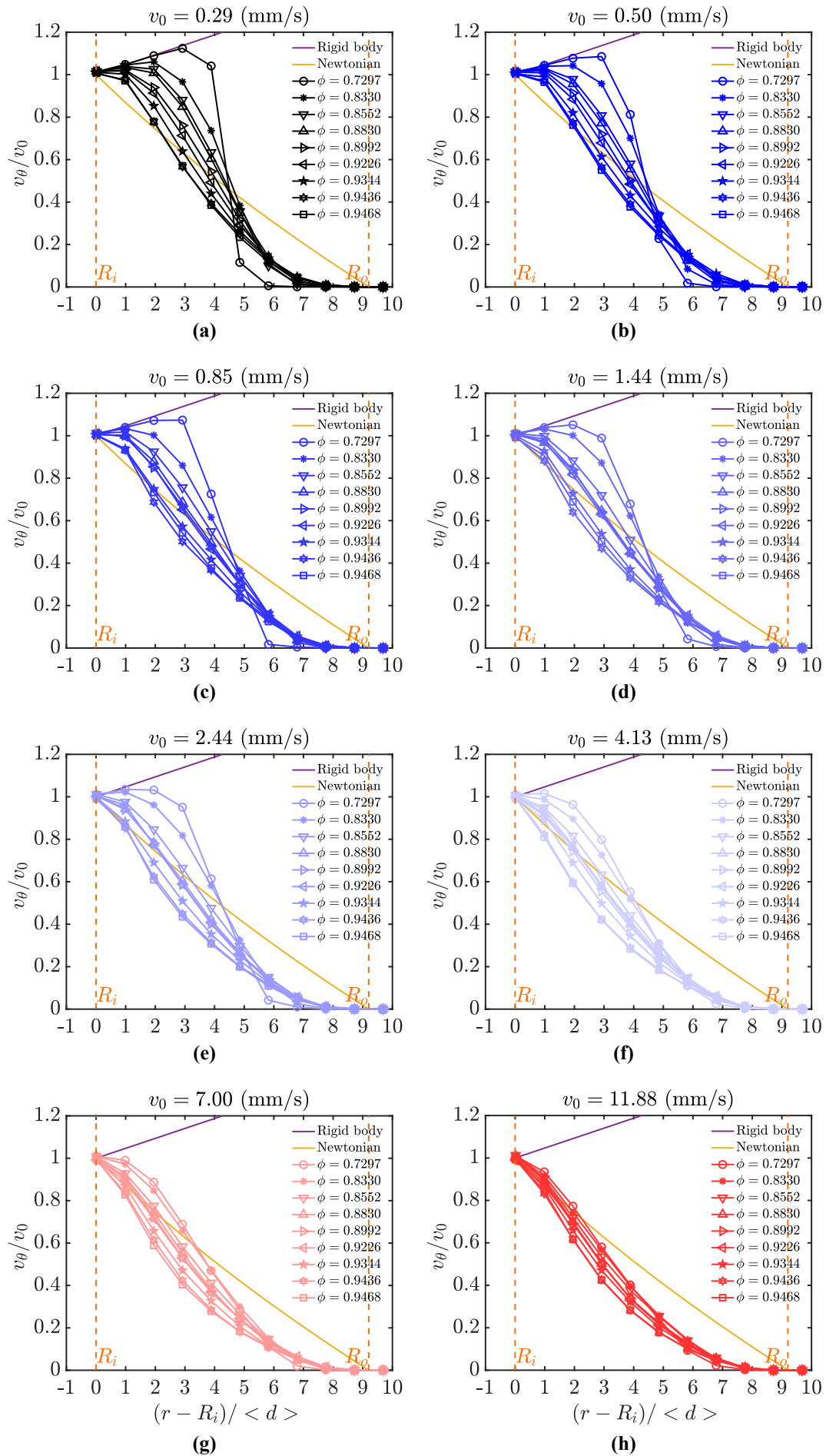


Figure 5.8: Velocity profiles for various droplet packings (represented by various symbols) at a given rotational speed (expressed by different colors).

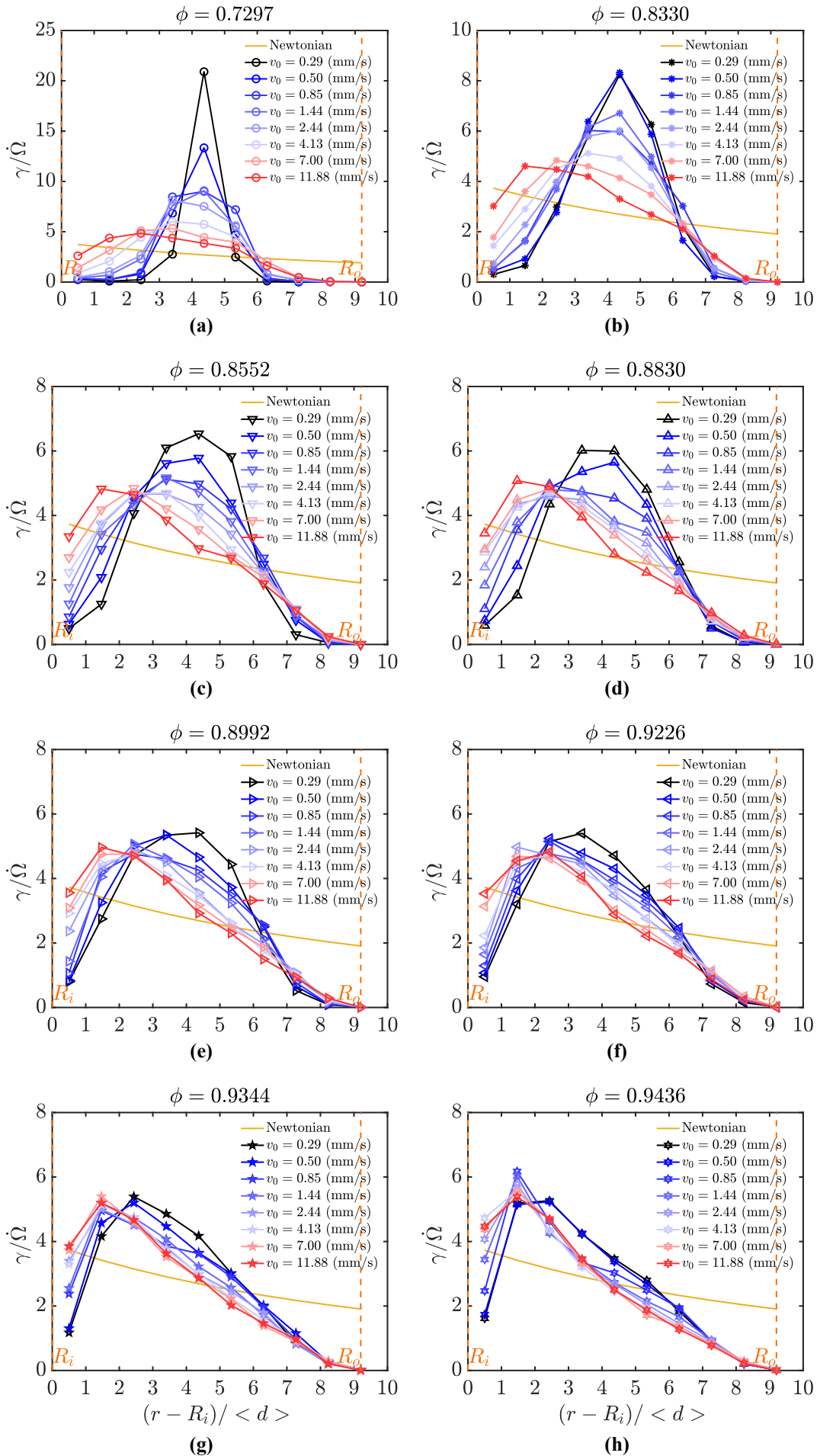


Figure 5.9: Local shear rates at different rotational speeds (represented by different colors) for a given droplet packing (expressed by various symbols).

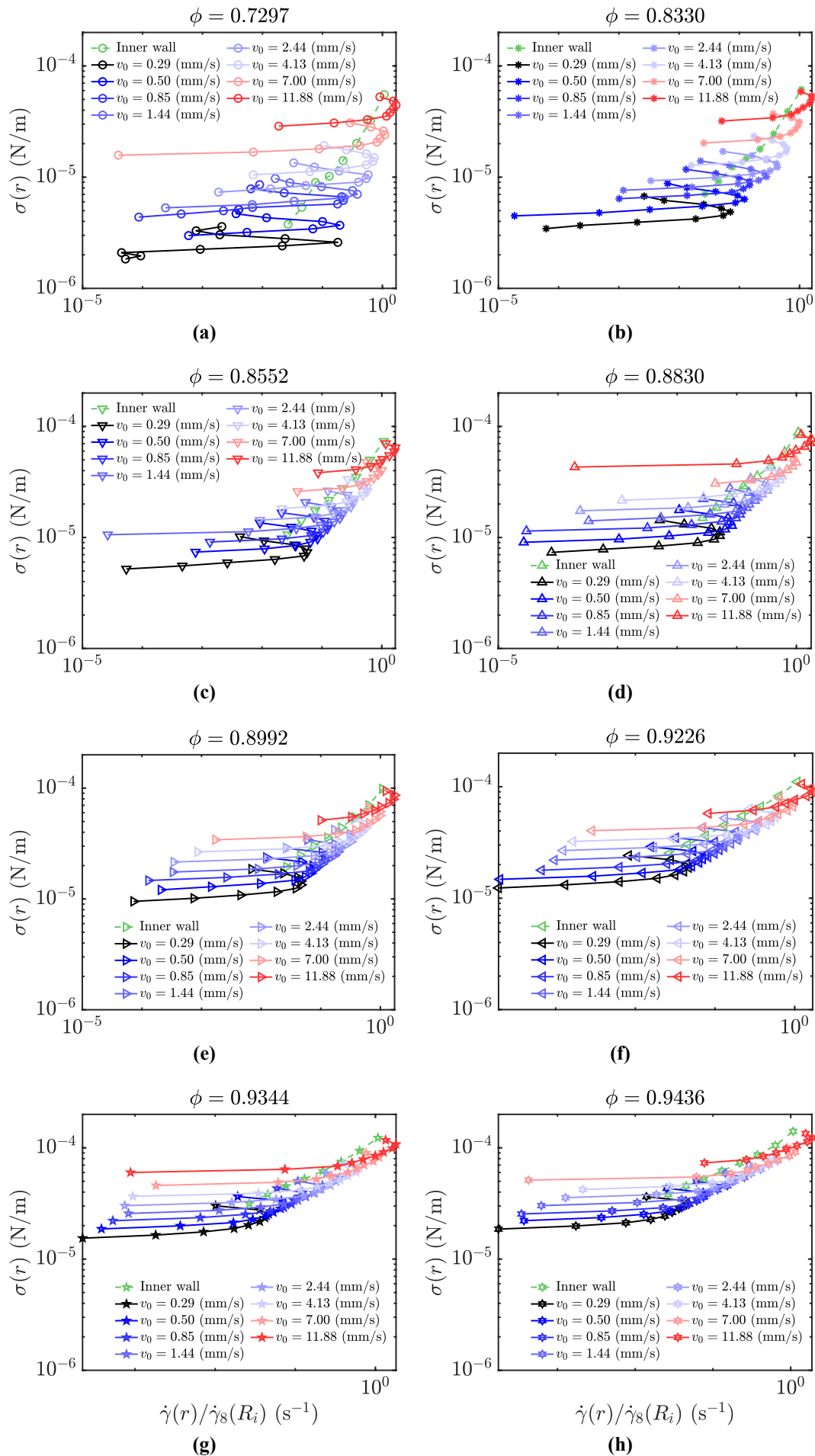


Figure 5.10: The local flow curves for various droplet packings.

Conclusion and Outlook

By reaching this point, we have achieved the first three research objectives outlined in Chapter 1. However, unexpected challenges like the non-local effect and the wall effect emerged during our research journey. The fourth objective, involving fitting macroscopic and local rheometrical data to a constitutive model and investigating the scaling analysis of flow curves, still lies ahead and requires a more detailed approach. In this chapter, we explore possible directions for the future research in terms of the experimental setup, the image analysis, and theoretical analysis.

Experimental setup

The current setup employs a cylindrical Couette ring to generate droplets and conduct rheological measurements within the same region. Although the monolayer is mixed at a constant rotational speed during the filling process, emulsion monolayer may be structured prior to the measurement depending on the rotation direction of the inner ring and the position of the two needles, which, however, could not be destructured by higher mixing velocities (e.g., 100 rpm) as droplets tend to coalesce at such velocities. In addition, some droplets are trapped by the walls, resisting further mixing. A potential solution involves decoupling the droplet generation process from rheological measurements. For example, we can first generate and mix droplets in a large squared reservoir where the wall effect is negligible and then direct the droplets into the Couette ring for measuring the rheology.

While a wider gap has been suggested to reduce the sensitivity of rheology to the non-local effect [53, 55], it is worth noting that the inner radius magnitude also plays a role [40]. Considering the droplet sizes generated in our experiments, it is important to explore various combinations of the inner radius R_i and the gap $R_o - R_i$ to understand the non-local effect better. For instance, in our current setup with $R_i / \langle d \rangle \approx 22$ and $(R_o - R_i) / \langle d \rangle \approx 9$, we can maintain $(R_o - R_i) / \langle d \rangle$ while conducting measurements with different values of $R_i / \langle d \rangle$, such as [12, 22, 32], to gain insights into the non-local effect. In addition, as the wall effect diffuses fast in radial direction (similar to a boundary layer), experimenting with different gap sizes also contributes to a deeper comprehension of the wall effect.

Concurrently, it is essential to develop methods to mitigate the wall effect. One approach is to modify the cross-shaped grooved structure of the inner ring to minimize the contact angle between the liquid interface and the wall. Additionally, applying coatings of specific materials to the inner ring could further decrease the contact angle. By implementing these strategies, the experiments can concentrate on investigating the local and macroscopic rheology of the emulsion monolayers, unobstructed by significant wall effects.

The absence of communication between the syringe pump and the rheometer hampers experiment repeatability, preventing consistent initiation with the same droplet packing for each trial. Therefore, a control system establishing connections between the pump, camera, and rheometer would facilitate more controlled and reproducible experiments.

Image analysis

Currently, the image analysis results are checked by the naked eye, lacking a quantitative assessment of resolution and error. While it is tricky to assess how accurately the detected centers represent the droplet positions, determining the method's resolution allows for filtering out displacements smaller than this resolution, enhancing data reliability. In addition, the current packing fraction results exhibit strong sensitivity to the binary threshold, implying an imaging acquisition with finer pixel sizes is in demand. On the other hand, while the current method works well in the middle region, it sometimes fails near the wall, as the droplets show different geometrical features between the middle and wall regions. A refined approach could involve employing two parallel procedures for separately detecting droplets in central and wall regions.

Theoretical analysis

A series of scaling analyses are recommended for quantifying the wall effect concerning:

- the shape and dimensions of an individual floating droplet. Considering a floating oil droplet at an air/water interface, the shape and dimensions of the droplet can be estimated if the magnitude of the densities ρ_o , ρ_w and ρ_a and the surface tensions T_{ow} , T_{oa} and T_{aw} are known. An approach reported by C.M. Phan et al. [57] offers a potential method.
- the capillary forces between droplets. As the buoyancy and the capillary force lead to the deformation of the liquid interface, droplets tend to approach each other. Evaluating inter-droplet forces could assist in developing relevant theoretical and simulation models. A suitable approach is outlined by G. Katgert in his doctoral thesis [58].
- The radial position-dependent scaling of the wall effect. The pronounced wall effect leads to faster movement of droplets near the inner wall than anticipated, diffusing rapidly within a few rows. If avoiding the wall effect is a challenge during the experiment, a scaling analysis would assist in estimating such external force applied to the monolayer. This analysis could contribute an additional term or modified boundary condition when formulating a constitutive model.

J. Goyon [55] formulated a widely employed non-local equation for the steady state:

$$f_{\text{bulk}} = f(r) - \xi^2 \frac{1}{r} \frac{\partial}{\partial r} \left(r \frac{\partial}{\partial r} f(r) \right), \quad (6.1)$$

where f_{bulk} is the bulk fluidity in a system with homogeneous shear stress and shear rate, and ξ is the cooperativity length characterizing the non-local effects. The diffusive term implies that spatial gradients induce deviations of the local fluidity f from the bulk fluidity. As the final objective is to describe system rheology via f_{bulk} , data should be fitted to estimate the cooperativity length. Furthermore, a comparison between the calculated bulk fluidity and macroscopic rheological measurements could reveal the feasibility of directly deducing the desired homogeneous bulk fluidity from macroscopic rheological data.

References

- [1] Fernando Leal-Calderon et al. *Emulsion science: basic principles*. Springer Science & Business Media, 2007.
- [2] Milton J Rosen et al. *Surfactants and interfacial phenomena*. John Wiley & Sons, 2012.
- [3] Schramm Laurier L. *Emulsions, Foams, and Suspensions Fundamentals and applications*. 2005.
- [4] Murtada Mohammed Abdulredha et al. “Overview on petroleum emulsions, formation, influence and demulsification treatment techniques”. In: *Arabian Journal of Chemistry* 13.1 (2020), pp. 3403–3428.
- [5] Howard A Barnes. “Rheology of emulsions—a review”. In: *Colloids and surfaces A: physicochemical and engineering aspects* 91 (1994), pp. 89–95.
- [6] Th F Tadros. “Fundamental principles of emulsion rheology and their applications”. In: *Colloids and Surfaces A: Physicochemical and Engineering Aspects* 91 (1994), pp. 39–55.
- [7] C Gallegos et al. “Rheology of food, cosmetics and pharmaceuticals”. In: *Current opinion in colloid & interface science* 4.4 (1999), pp. 288–293.
- [8] Morton M Denn et al. “Issues in the flow of yield-stress liquids”. In: *Rheologica acta* 50 (2011), pp. 307–315.
- [9] Kerstin N Nordstrom et al. “Microfluidic rheology of soft colloids above and below jamming”. In: *Physical review letters* 105.17 (2010), p. 175701.
- [10] José Paredes et al. “Rheology across the zero-temperature jamming transition”. In: *Physical review letters* 111.1 (2013), p. 015701.
- [11] Anindita Basu et al. “Rheology of soft colloids across the onset of rigidity: scaling behavior, thermal, and non-thermal responses”. In: *Soft matter* 10.17 (2014), pp. 3027–3035.
- [12] M Dinkgreve et al. “Universal rescaling of flow curves for yield-stress fluids close to jamming”. In: *Physical Review E* 92.1 (2015), p. 012305.
- [13] Peter Olsson et al. “Critical scaling of shear viscosity at the jamming transition”. In: *Physical review letters* 99.17 (2007), p. 178001.
- [14] Brian P Tighe et al. “Model for the scaling of stresses and fluctuations in flows near jamming”. In: *Physical review letters* 105.8 (2010), p. 088303.
- [15] Simon Dagois-Bohy et al. “Softening and yielding of soft glassy materials”. In: *Soft matter* 13.47 (2017), pp. 9036–9045.
- [16] Riande I Dekker et al. “Scaling of flow curves: Comparison between experiments and simulations”. In: *Journal of non-Newtonian fluid mechanics* 261 (2018), pp. 33–37.

- [17] John Lauridsen et al. “Velocity profiles in slowly sheared bubble rafts”. In: *Physical Review Letters* 93.1 (2004), p. 018303.
- [18] Yuhong Wang et al. “Impact of boundaries on velocity profiles in bubble rafts”. In: *Physical review E* 73.3 (2006), p. 031401.
- [19] Gijs Katgert et al. “Flow in linearly sheared two-dimensional foams: From bubble to bulk scale”. In: *Physical Review E* 79.6 (2009), p. 066318.
- [20] Steven Vandebril et al. “A double wall-ring geometry for interfacial shear rheometry”. In: *Rheologica Acta* 49 (2010), pp. 131–144.
- [21] Malvern. *Introduction to Rheology*. 2016. URL: <https://cdn.technologynetworks.com/TN/Resources/PDF/WP160620BasicIntroRheology.pdf>. (accessed: 05.9.2022).
- [22] Malcolm M Cross. “Rheology of non-Newtonian fluids: a new flow equation for pseudo-plastic systems”. In: *Journal of colloid science* 20.5 (1965), pp. 417–437.
- [23] AW Sisko. “The flow of lubricating greases”. In: *Industrial & Engineering Chemistry* 50.12 (1958), pp. 1789–1792.
- [24] Winslow H Herschel et al. “Konsistenzmessungen von gummi-benzollösungen”. In: *Kolloid-Zeitschrift* 39 (1926), pp. 291–300.
- [25] Christopher W Macosko. “Rheology principles”. In: *Measurements and Applications* (1994).
- [26] HA Barnes et al. “The yield stress myth?” In: *Rheologica acta* 24 (1985), pp. 323–326.
- [27] Francesca Ravera et al. “Emulsification and emulsion stability: The role of the interfacial properties”. In: *Advances in Colloid and Interface Science* 288 (2021), p. 102344.
- [28] Albert Einstein. “Eine neue bestimmung der moleküldimensionen”. PhD thesis. ETH Zurich, 1905.
- [29] Irvin M Krieger et al. “A mechanism for non-Newtonian flow in suspensions of rigid spheres”. In: *Transactions of the Society of Rheology* 3.1 (1959), pp. 137–152.
- [30] Howard A Barnes et al. *An introduction to rheology*. Vol. 3. Elsevier, 1989.
- [31] Ronald G Larson. *The structure and rheology of complex fluids*. Vol. 150. Oxford university press New York, 1999.
- [32] Takahiro Hatano. “Scaling properties of granular rheology near the jamming transition”. In: *Journal of the Physical Society of Japan* 77.12 (2008), p. 123002.
- [33] Michio Otsuki et al. “Critical behaviors of sheared frictionless granular materials near the jamming transition”. In: *Physical Review E* 80.1 (2009), p. 011308.
- [34] Corey S O’hern et al. “Jamming at zero temperature and zero applied stress: The epitome of disorder”. In: *Physical Review E* 68.1 (2003), p. 011306.
- [35] Gijs Katgert et al. “The jamming perspective on wet foams”. In: *Soft Matter* 9.41 (2013), pp. 9739–9746.
- [36] Carl P Goodrich et al. “Jamming in finite systems: Stability, anisotropy, fluctuations, and scaling”. In: *Physical Review E* 90.2 (2014), p. 022138.

- [37] Georges Debregeas et al. “Deformation and flow of a two-dimensional foam under continuous shear”. In: *Physical Review Letters* 87.17 (2001), p. 178305.
- [38] William Lawrence Bragg et al. “A dynamical model of a crystal structure”. In: *Proceedings of the Royal Society of London. Series A. Mathematical and Physical Sciences* 190.1023 (1947), pp. 474–481.
- [39] M Fátima Vaz et al. “Experiments on defect spreading in hexagonal foams”. In: *Journal of Physics: Condensed Matter* 9.42 (1997), p. 8921.
- [40] Gijs Katgert et al. “Couette flow of two-dimensional foams”. In: *Europhysics Letters* 90.5 (2010), p. 54002.
- [41] John Lauridsen et al. “Shear-induced stress relaxation in a two-dimensional wet foam”. In: *Physical review letters* 89.9 (2002), p. 098303.
- [42] Christopher Gilbreth et al. “Flow transitions in two-dimensional foams”. In: *Physical Review E* 74.5 (2006), p. 051406.
- [43] Philippe Coussot et al. “Coexistence of liquid and solid phases in flowing soft-glassy materials”. In: *Physical review letters* 88.21 (2002), p. 218301.
- [44] Stéphane Rodts et al. “From “discrete” to “continuum” flow in foams”. In: *Europhysics Letters* 69.4 (2005), p. 636.
- [45] E Janiaud et al. “Two-dimensional foam rheology with viscous drag”. In: *Physical review letters* 97.3 (2006), p. 038302.
- [46] Gijs Katgert et al. “Rate dependence and role of disorder in linearly sheared two-dimensional foams”. In: *Physical review letters* 101.5 (2008), p. 058301.
- [47] Gerald G Fuller et al. “Complex fluid-fluid interfaces: rheology and structure”. In: *Annual review of chemical and biomolecular engineering* 3 (2012), pp. 519–543.
- [48] Daniel K Schwartz et al. “Direct observation of Langmuir monolayer flow through a channel”. In: *Physical review letters* 73.21 (1994), p. 2841.
- [49] Carlton F Brooks et al. “An interfacial stress rheometer to study rheological transitions in monolayers at the air- water interface”. In: *Langmuir* 15.7 (1999), pp. 2450–2459.
- [50] Joseph A Zasadzinski et al. “The physics and physiology of lung surfactants”. In: *Current Opinion in Colloid & Interface Science* 6.5-6 (2001), pp. 506–513.
- [51] Dominic Vella et al. “The “cheerios effect””. In: *American journal of physics* 73.9 (2005), pp. 817–825.
- [52] Gijs Katgert et al. “Jamming and geometry of two-dimensional foams”. In: *Europhysics Letters* 92.3 (2010), p. 34002.
- [53] Guillaume Ovarlez et al. “Wide-gap Couette flows of dense emulsions: Local concentration measurements, and comparison between macroscopic and local constitutive law measurements through magnetic resonance imaging”. In: *Physical Review E* 78.3 (2008), p. 036307.
- [54] Nicolas Huang et al. “Viscosity of a dense suspension in Couette flow”. In: *Journal of fluid mechanics* 590 (2007), pp. 497–507.

-
- [55] Julie Goyon et al. “Spatial cooperativity in soft glassy flows”. In: *Nature* 454.7200 (2008), pp. 84–87.
- [56] Guillaume Ovarlez et al. “On the existence of a simple yield stress fluid behavior”. In: *Journal of Non-Newtonian Fluid Mechanics* 193 (2013), pp. 68–79.
- [57] Chi M Phan et al. “Can water float on oil?” In: *Langmuir* 28.10 (2012), pp. 4609–4613.
- [58] Gijs Katgert. “Flow of foams”. PhD thesis. Doctoral Dissertation, Universiteit Leiden, 2008.